

BRNO UNIVERSITY OF TECHNOLOGY
VYSOKÉ UČENÍ TECHNICKÉ V BRNĚ



FACULTY OF MECHANICAL ENGINEERING
INSTITUTE OF PHYSICAL ENGINEERING

FAKULTA STROJNÍHO INŽENÝRSTVÍ
ÚSTAV FYZIKÁLNÍHO INŽENÝRSTVÍ

DESIGN AND VERIFICATION OF LOW TEMPERATURE
PART OF UHV – STM MICROSCOPE
NÁVRH A OVĚŘENÍ NÍZKOTEPLTNÍ ČÁSTI UHV - STM MIKROSKOPU

MASTER'S THESIS
DIPLOMOVÁ PRÁCE

AUTHOR
AUTOR PRÁCE

Bc. JAKUB VOŇKA

SUPERVISOR
VEDOUCÍ PRÁCE

Ing. PAVEL URBAN, Ph.D.

BRNO 2013



This diploma thesis was elaborated at the
Institute of Scientific Instruments of the AS CR, v. v. i.

based on the Contract of scientific collaboration, No: 0313220 03950,
between
the Institute of Scientific Instruments of the AS CR, v. v. i.
and
the Faculty of Mechanical Engineering of Brno University of Technology.

under supervision of:
Ing. Pavel Urban, Ph.D.

Vysoké učení technické v Brně, Fakulta strojního inženýrství

Ústav fyzikálního inženýrství

Akademický rok: 2012/2013

ZADÁNÍ DIPLOMOVÉ PRÁCE

student(ka): Bc. Jakub Voňka

který/která studuje v **magisterském navazujícím studijním programu**

obor: **Fyzikální inženýrství a nanotechnologie (3901T043)**

Ředitel ústavu Vám v souladu se zákonem č.111/1998 o vysokých školách a se Studijním a zkušebním řádem VUT v Brně určuje následující téma diplomové práce:

Návrh a ověření nízkoteplotní části UHV - STM mikroskopu

v anglickém jazyce:

Design and verification of low temperature part of UHV – STM microscope

Stručná charakteristika problematiky úkolu:

Cílem práce je navrhnout a ověřit nízkoteplotní část UHV - STM mikroskopu, který bude pracovat při proměnné teplotě vzorku v rozsahu 20 K - 300 K. Vzhledem k požadavku na proměnnou teplotu vzorku bude použit heliový průtokový systém chlazení s využitím studeného He (~ 5 K) jako chladiva. Navrhovaný systém bude sestávat z chlazeného nosiče vzorků, přívodů He, tepelných výměníků a Cu svazků (tzv. „braidů“) pro tepelnou vazbu nosiče vzorků a tepelně izolačních štítů kolem stolku mikroskopu. Bude vypracován způsob uložení chlazeného nosiče vzorku s požadavkem na nízkou tepelnou vodivost a současně mechanickou tuhost, který bude teoreticky analyzován a experimentálně ověřen ve zkušební vakuové komoře. Dále bude řešeno tepelné kontaktování vzorků, měření teploty vzorků a přenos vibrací na vzorek. Téma bude řešeno ve spolupráci s Ústavem přístrojové techniky AV ČR, v.v.i. v Brně.

Cíle diplomové práce:

Návrh a ověření nízkoteplotní části UHV - STM mikroskopu, který bude pracovat při proměnné teplotě vzorku v rozsahu 20 K - 300 K.

ABSTRACT

The diploma thesis addresses the design and experimental verification of a cooling system and low temperature part of an UHV-STM working in temperature range of 20 K–300 K. Due to the demand of variable temperature, the flow cooling system with cryogenic (~ 5 K) helium (He) is used. Two variants of the low temperature part of the microscope are studied, the first one with cooled sample holder only, and the second one with cooling of the whole STM. Designed cooling system consists of a He flow cryostat allowing to connect it to a Dewar vessel containing liquid helium (LHe) with a low-loss transfer line. The cryostat consists of He inlet and outlet, heat exchangers and copper strands (so called braids) for the thermal connection of both the sample holder/STM and the radiation shield around the STM with the heat exchangers. The thesis describes the design, heat flow analysis and initial tests of the flow cryostat in the designed vacuum chamber. Heat flow through a spot contact is also discussed to estimate the thermal conductance of insulation supports based on thermal resistance of spherical contacts. The thesis was elaborated in collaboration with the Institute of Scientific Instruments of the ASCR, v.v.i.

KEYWORDS

flow LHe cryostat, LT-STM, cryogenics

ABSTRAKT

Diplomová práce se zabývá návrhem a ověřením chladicího systému a nízkoteplotní části UHV-STM mikroskopu, který bude pracovat při proměnné teplotě vzorku v rozsahu 20 K–300 K. Vzhledem k požadované proměnné teplotě je použito heliového průtokového systému chlazení s využitím studeného He (~ 5 K) jako chladiva. Jsou řešeny dvě varianty nízkoteplotní části mikroskopu, v první verzi je chlazen pouze nosič vzorků, v druhém verzi je chlazen celý STM mikroskop. Navržený chladicí systém tvoří He průtokový kryostat, který umožňuje připojení k zásobníku kapalného He (LHe) prostřednictvím nízkoztrátového He přepouštěče. Kryostat sestává z přívodů He, tepelných výměníků a měděných svazků (tzv. "braidů") pro tepelnou vazbu tepelných výměníků s nosičem vzorků/STM a s tepelně izolačním štítem kolem stolku mikroskopu. V práci je popsán návrh a konstrukce průtokového kryostatu s prvotními testy v sestavené vakuové komoře. Dále je zde detailní rozbor tepelných toků tepelně izolačními podpěrami založenými na styku sférických ploch a analýza tepelných toků v nízkoteplotní části chlazeného STM mikroskopu. Téma bylo řešeno ve spolupráci s Ústavem přístrojové techniky AV ČR, v.v.i. v Brně.

KLÍČOVÁ SLOVA

průtokový LHe kryostat, LT-STM, kryogenika

VOŇKA, Jakub *Design and verification of low temperature part of UHV – STM microscope*: master's thesis. Brno: Brno University of Technology, Faculty of Mechanical Engineering, Institute of Physical Engineering, 2013. 63 p. Supervised by Ing. Pavel Urban, Ph.D.

DECLARATION

I declare that I have written my master's thesis on the theme of "Design and verification of low temperature part of UHV – STM microscope" independently, under the guidance of the master's thesis supervisor and using the technical literature and other sources of information which are all quoted in the thesis and detailed in the list of literature at the end of the thesis.

As the author of the master's thesis I furthermore declare that, as regards the creation of this master's thesis, I have not infringed any copyright. In particular, I have not unlawfully encroached on anyone's personal and/or ownership rights and I am fully aware of the consequences in the case of breaking Regulation § 11 and the following of the Copyright Act No 121/2000 Sb., and of the rights related to intellectual property right and changes in some Acts (Intellectual Property Act) and formulated in later regulations, inclusive of the possible consequences resulting from the provisions of Criminal Act No 40/2009 Sb., Section 2, Head VI, Part 4.

Brno

.....

(author's signature)

ACKNOWLEDGMENTS

I would like to express my thanks to Pavel Hanzelka and Pavel Urban for guiding this thesis and many valuable advice, whole Group of Cryogenics and Superconductivity for pleasant and originative environment, and my parents for their loving support.

CONTENTS

Introduction	3
1 Theory	5
1.1 Helium	5
1.1.1 Helium properties	5
1.2 Heat transport mechanisms	6
1.2.1 Radiative heat transfer	7
1.2.2 Thermal conductivity	10
1.3 Specific heat	12
1.4 Thermal expansion	14
1.5 Mechanical properties at low temperatures	16
2 LT-STM platform with cooled sample holder	18
3 Flow cooling system	20
3.1 Helium inlet and outlet	21
3.1.1 Inlet tube calculation	23
3.1.2 Anchoring the braid on output tube	24
3.2 Heat exchangers	25
3.2.1 Assembly	25
3.2.2 Calculations	27
3.3 Testing vacuum chamber	29
3.4 Tests of the cooling system	30
3.4.1 Pressure drop measurement	30
3.4.2 First cooldowns	31
3.4.3 Test with the new transfer line	33
4 Four ball supports	34
4.1 Description of the support	34
4.2 Spot contact	35
4.2.1 The simplest model	35
4.2.2 Numerical model	36
4.2.3 Model with flat isothermal contact area	39
4.3 Testing application of the FBS	40
4.3.1 Cooldowns	41
4.3.2 Temperature fluctuations and LHe consumption	42
4.3.3 Heat flow analysis	44
4.3.4 Mechanical stiffness measurement	45

5	New design of the STM platform	48
5.1	Steady state heat flow calculation	49
5.2	Cooldown time calculation	56
6	Conclusions	59
	List of symbols, physical constants and abbreviations	62

LIST OF FIGURES

1.1	Monochromatic emissive power of a blackbody.	7
1.2	Radiative heat flow between two parallel surfaces.	9
1.3	Radiative heat flow for coaxial cylinders or enclosed spheres.	10
1.4	Thermal conductivity of some common cryogenic materials.	12
1.5	Heat capacity of some common cryogenic materials.	14
1.6	Lennard-Jones potential.	15
1.7	Elongation of various materials with temperature.	16
2.1	The scheme of the STM platform with scanning head at room temperature.	19
3.1	The scheme showing the principle of the flow cooling.	20
3.2	The flow cryostat without heat exchangers.	22
3.3	Input tube heat calculation scheme.	24
3.4	Input tube temperature profiles.	24
3.5	The design of the anchor of the braid on the output tube.	25
3.6	The section view of the heat exchanger assembly.	26
3.7	Three main parts of the heat exchanger.	27
3.8	Testing vacuum chamber with the flow cryostat.	30
3.9	Pressure loss measurement with room temperature helium gas.	31
4.1	Principle of the four ball support.	34
4.2	The first model for calculation of heat flow through a spot contact.	35
4.3	Scheme of the numerical model of the spot contact calculation.	36
4.4	Numerical model of the spot contact calculation.	37
4.5	Calculated temperature distributions around the spot contact.	38
4.6	Calculated temperature profile of the spot contact.	38
4.7	Model with flat isothermal contact area.	39
4.8	Measured and calculated thermal conductivity of the spherical support.	40
4.9	Sample holder dummy.	41
4.10	Cooldown of the dummy sample holder.	42
4.11	Thermal oscillations.	43
4.12	The dummy sample holder suspended on polyester fibers.	45
4.13	The apparatus for measurement of mechanical stiffness	46
4.14	Dependence of deflection on lateral force.	47
4.15	Measured dependence of mechanical stiffness on the preload.	47
5.1	Schematic representation of the LT-STM platform.	49
5.2	The scheme of the calculated model of LT-STM.	50
5.3	Comparison of capacity of the sample holder dummy and the STM.	57

LIST OF TABLES

1.1	Some important physical properties of ^4He	6
1.2	Importance of latent heat for cooldown.	6
1.3	Values of absorptivity for various materials.	8
1.4	Debye temperature Θ_D of some elements and substances.	13
3.1	Basic parameters of the heat exchangers.	29
3.2	Results of the test with the old transfer line.	32
3.3	Results of the tests with the new transfer line.	33
4.1	Convenient consumption and fluctuations amplitudes.	43
4.2	Heat flow analysis of sample holder dummy.	45
5.1	Parasitic heat flow calculation for some commercially available cryo- genic wires.	53
5.2	Parasitic heat flow calculation for some commercially available cryo- genic mini-coaxial cables.	53
5.3	Calculated parasitic heat flows on the STM block.	55
5.4	Calculated parasitic heat flows to the radiation shield.	55
5.5	Calculated cooldown times and final temperatures of the STM core.	58

INTRODUCTION

This thesis addresses low temperature parts of a scanning tunneling microscope (STM) together with a flow cooling system with liquid helium (LHe) designed in the Group of Cryogenics and Superconductivity at the Institute of Scientific Instruments (ISI). The low temperature STM (LT-STM) with atomic resolution will be used for studying nanostructures in the variable temperature range of 20 K to 300 K and will be utilized in the existing ultra-high vacuum (UHV) chamber at the Institute of Physical Engineering (IPE) at Brno University of Technology.

Due to the demand of variable temperature of the sample, one of the suitable solutions is to use a flow cooling with changing the temperature by regulating the flow rate of coolant. Cooling under 80 K requires the use of liquid helium with boiling point at normal pressure at 4.2 K. Helium is led from a storage vessel (Dewar vessel) to the heat exchangers which serve to cool the sample holder and possibly the radiation shield around it. Helium streams through the heat exchangers as liquid, gas or as a mixture of both phases. The samples are placed either directly on the heat exchanger or are thermally linked with the heat exchanger with highly conductive fine copper wires, so called braids. The lowest reachable temperature depends on the system design, i. e. thermal link of the sample holder to the heat exchanger, quality of the thermal contact of the sample, shielding against parasitic heat flows, etc. Commercially available variable temperature STM systems with LHe reach the lowest temperature of about 2 K (by pumping the He vapor) where the sample is attached directly to the heat exchangers [1] and about 25 K if thermal connection to the sample holder is realized by braids [2, 3]. Our case will require the variant with braids and a two stage system - cooling of the sample and the radiation shield around it.

This work is a direct continuation of my bachelor thesis [4], which deals with the selection of materials for their potential application in the low temperature parts of the LT-STM and with the study of available braids focused on their thermal conductivity. Furthermore, the design of insulating supports for the fixation of the sample holder on the table at room temperature based on the spot contact between glass balls is explained there.

Chapter 1 introduces the properties of cryogenic helium as well as the cryogenic properties of materials used in the flow cooling system and outlines the implications of the discussed properties on the designed low temperature apparatus. Heat transport mechanisms at cryogenic temperatures needed for the calculations of the heat flows in the designed system are also described. The setup of the LT-STM platform with cooled sample holder and scanning head at room temperature is briefly presented in chapter 2. Next chapter 3 describes the design of the flow cooling system

and especially the design of the cryostat consisting of He inlet/outlet and the heat exchangers. The vacuum chamber designed and built for testing of the cryostat is also mentioned. The results of initial tests are presented in the last part of this chapter. The following chapter 4 links to my bachelor thesis [4] and continues to characterize the insulating supports, especially the study of the heat flow through the spot contacts. This part was performed in close collaboration with P. Hanzelka who designed the supports and V. Musilová who derived the relations for heat flow through a spot contact. The obtained results are already in review process for publishing in Review of Scientific Instruments [5]. The last chapter 5 outlines the new design with both scanning head and sample holder at low temperature. Solution of possible mounting of the microscope inside the vacuum chamber on the table insulated from vibrations is proposed and the analysis of heat flows is performed and obtained results are commented.

The work was done within the Group of Cryogenics and Superconductivity at the Institute of Scientific Instruments of the ASCR, v.v.i. in Brno. The experimental setups were built and tested in close collaboration with P. Hanzelka. Cryogenic calculations and principles of the cooling setup were discussed with both P. Hanzelka and P. Urban.

1 THEORY

When designing the STM flow cooling, it is necessary to keep in mind the specifics of cryogenic temperatures. Material properties at low temperatures often significantly differ from those at room temperature and changes of values by even a few orders of magnitude after cooling down are not uncommon. Being aware of these specific aspects is thus very important for cryogenic calculations and proper design of the flow cryostat.

1.1 Helium

For cooling below the temperature of the boiling point of liquid nitrogen, 77 K at normal pressure, liquid helium (LHe) is usually used as a coolant due to its lowest boiling point of all technical gases, 4.2 K. Since the lowest temperature desired in the developed STM is about 20 K, cooling by LHe will be utilized. Helium exists in two stable isotopes: normal ^4He and much more rare ^3He with extensive use in sub-Kelvin temperature range. While the designed flow cooling will only work with the ^4He , this thesis restrains to this isotope only and refers to it as “helium”.

1.1.1 Helium properties

Helium is a rare gas (only $5 \times 10^{-4}\%$ of mass in atmosphere) that is the hardest of all to liquify. Table 1.1 shows some physical properties significant for the flow cooling. Most important value to point out is the latent heat of evaporation of LHe, which is very small compared to its enthalpy to room temperature. For illustration, 1 W will evaporate 1.39 l/h of LHe when using only heat of evaporation. The same 1 W will evaporate only 0.02 l/h of LHe if the enthalpy to room temperature is utilized. As a result, it is very important that the cooling power of remaining cold helium gas is used as well with the heat of evaporation. In order to reduce the LHe consumption in a flow cryostat, helium gas should leave the cooling apparatus as close to room temperature as possible. The Table 1.2 expresses the phenomenon in a similar way showing how many liters of LHe are needed in order cool down 1 kg of material.

Another property to keep in mind is the room temperature gas to liquid volume ratio. When helium evaporates, its volume increases more than 700 times. This is of key importance in cryostat design, especially for safety reasons. Even though the density of cold helium gas at 5 K is lower only 10 times compared to LHe, in case of the flow cryostat, the expansion of gas can create strong vibrations on places where helium boils (heat exchangers, thin-walled capillaries etc.). The gas expansion also often causes temperature fluctuations on heat exchangers and will be

further discussed in one of the following chapters as this effect was also encountered in the designed flow cryostat.

Dynamic viscosity of liquid helium is about 1000 times lower than that of water and about 100 times lower than that of liquid nitrogen. Viscosity of 5 K helium vapor is only about 2 times lower than that of liquid.

Tab. 1.1: Some important physical properties of ^4He . All of the properties are referring to normal pressure. Data from [6, 7, 8].

Boiling point	4.21 K
Density of liquid	125 kg/m ³
Latent heat of evaporation	20.7 kJ/kg
Enthalpy (4.2 K to 77 K) ¹	405 kJ/kg
Enthalpy (4.2 K to 300 K) ¹	1563 kJ/kg
Gas to liquid volume ratio ²	757
Dynamic viscosity of liquid ³	3.26×10^{-6} Pa s
Dynamic viscosity of gas ⁴	1.26×10^{-6} Pa s
Specific heat at constant pressure ⁴	6.7 kJ/kg K
Specific heat at constant pressure ⁵	5.2 kJ/kg K

¹Without heat of evaporation.

²Liquid at 4.2 K, gas at 300 K.

³Liquid at 4 K.

⁴Gas at 5 K.

⁵Gas from 20 K to 300 K.

Tab. 1.2: Amount of liquid helium needed in order to cool down a kilogram of a material from 300 K to 4.2 K with and without latent heat of cold helium gas. Calculation based on data from [6].

	Pb	In	Cu	Al	
Only heat of evaporation	12	22	31	66	liters of LHe
Including latent heat	0.2	0.3	0.4	0.9	liters of LHe

1.2 Heat transport mechanisms

Two major heat transport mechanisms that play significant role in calculation of the heat flows in the UHV LHe cryostat are discussed in this section: the heat transfer by radiation and by conduction. There are other mechanisms of heat transfer

encountered in cryogenics, such as heat transport by residual gas molecules. In the pressure range of about 10^{-4} Pa to 10^{-6} Pa the heat exchange is comparable with other heat transfer mechanisms, but for pressures lower than 10^{-6} Pa it can be neglected. Because the vacuum space of the flow cryostat will be connected with the UHV chamber, the pressure inside it will be well below 10^{-6} Pa.

1.2.1 Radiative heat transfer

Radiative heat transfer takes place in form of electromagnetic waves in a wide range of wavelengths. For a blackbody, the energy emitted per unit surface area at a specific wavelength λ is described by the Planck's radiation law in terms of the monochromatic emissive power [9]

$$E_\lambda(T) = \frac{C_1}{\lambda^5 [\exp(C_2/\lambda T) - 1]}, \quad (1.1)$$

where T is the temperature of the blackbody and C_1 and C_2 are so called radiation constants

$$C_1 = 2\pi hc^2 \doteq 3.7415 \times 10^{-16} \text{ W m}^2 \quad (1.2a)$$

$$C_2 = hc/k_B \doteq 1.4388 \times 10^{-2} \text{ K m}. \quad (1.2b)$$

h represents the Planck constant, c the speed of light and k_B the Boltzmann constant. Fig. 1.1 shows the dependence of E_λ on λ for a few temperatures. It is evident that a body at given temperature emits the radiation mainly around one specific wavelength λ_m , which corresponds to the maximum on the emissive power curve. We can find λ_m simply by setting derivation of the Planck's law with respect to

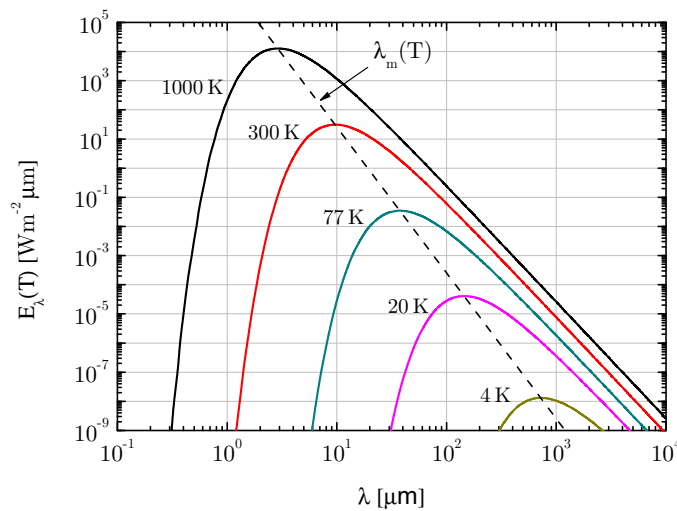


Fig. 1.1: Monochromatic emissive power of a blackbody as a function of wavelength.

wavelength to zero and obtain the Wien displacement law

$$\lambda_m = \frac{2898}{T} \quad (\mu\text{m}, \text{K}). \quad (1.3)$$

Radiative heat flow q_R can be derived by integration of Planck's law and thus Stefan–Boltzmann law is obtained

$$q_R = \sigma T^4, \quad (1.4)$$

where σ is the Stefan-Boltzmann constant.

No real material behaves like a blackbody, thus for a real material the right hand side of the equation (1.4) needs to be multiplied by the emissivity coefficient ε . It describes the ability of a surface to emit energy by radiation relative to that of a blackbody. Real material also does not absorb all of the radiation, so similarly an absorptivity coefficient a is used, defined as the ratio of the radiative heat flux absorbed by the material to the heat flux absorbed by a blackbody. When a material is in a thermal equilibrium with its surrounding, emissivity and absorptivity are equal. (If the two differed, there could be a net heat flow between two bodies at same temperature resulting in violation of the second law of thermodynamics.) Typical values of absorptivity for a few common materials with various surface treatment are listed in Tab. 1.3. Normally, the absorptivity decreases with decreasing temperature of the radiation source. There is a strong dependence on surface treatment of the material, however only a weak dependence on the temperature of the absorbing material.

Tab. 1.3: Values of absorptivity a in % for various materials at ~ 5 K for three different temperatures of a radiating blackbody. Data from [10, 11].

Material	300 K	150 K	4 K
Al, chemically polished	1.0	0.7	0.3
AlCu (AA2024)	3.0	2.0	0.7
Cu, abraded	1.9	1.3	0.7
Cu, chemically polished	0.6	0.5	0.3
Cu, old surface	2.6	1.5	0.4
Stainless steel, finely turned	6.0	2.2	–

For usual applications, heat flow between two surfaces S_1 and S_2 at temperatures T_1 and T_2 is more important than the heat flow that body radiates to its surroundings and is defined as follows

$$Q_{21r} = \sigma E_{21} S_{21} (T_2^4 - T_1^4), \quad (1.5)$$

where E_{21} is the coefficient of mutual emissivity takes into account the emissivities of both materials and the geometry.

Equation (1.5) tell us that the parts cooled with LHe should never be exposed to even small surfaces at room temperature. For illustration, heat radiated from 10 cm^2 equals to 0.5 W , which evaporates 0.71 l/h of LHe. The same area at temperature of boiling nitrogen (77 K) radiates heat flow of only 2 mW and reduces the LHe evaporation to 3 ml/h .

Radiation between two parallel surfaces

In case of two parallel infinite surfaces shown in Fig. 1.2 the mutual emissivity coefficient has the form

$$E_{21} = \frac{\varepsilon_1 \varepsilon_2}{\varepsilon_2 + (1 - \varepsilon_2) \varepsilon_1} = \frac{1}{\frac{1}{\varepsilon_1} + \frac{1}{\varepsilon_2} - 1}. \quad (1.6)$$

Moreover, for the two common cases below E_{21} further reduces to

$$\varepsilon_1 \ll \varepsilon_2 : E_{21} = \varepsilon_1, \quad (1.7a)$$

$$\varepsilon_1 = \varepsilon_2 = \varepsilon \ll 1 : E_{21} = \varepsilon/2. \quad (1.7b)$$

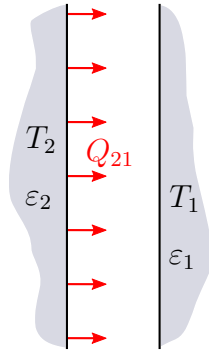


Fig. 1.2: Radiative heat flow between two parallel surfaces.

Radiation from a surrounding body

Another very common case are two coaxial cylinders or spherical enclosures, see Fig. 1.3. The coefficient S_{21} reduces to S_1

$$Q_{21} = \sigma E_{21} S_1 (T_2^4 - T_1^4) \quad (1.8)$$

and the mutual emissivity coefficient has the form

$$E_{21} = \frac{\varepsilon_1 \varepsilon_2}{\varepsilon_2 + (S_1/S_2) (1 - \varepsilon_2) \varepsilon_1} \quad (1.9)$$

when the surroundings has much greater surface or its emissivity is close to unity, the mutual emissivity coefficient further reduces to

$$\varepsilon_2 \sim 1 : E_{21} = \varepsilon_1, \quad (1.10a)$$

$$S_1 \ll S_2 : E_{21} = \varepsilon_1. \quad (1.10b)$$

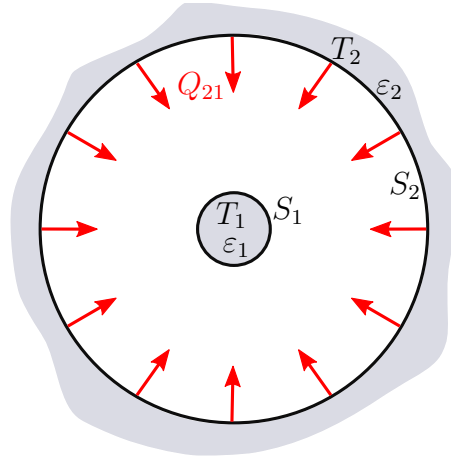


Fig. 1.3: Radiative heat flow for coaxial cylinders or enclosed spheres.

Radiative heat flow through an orifice

For calculation of radiative heat flow to a closed volume through an orifice, usually we consider the mutual emissivity coefficient E_{21} as unity. The radiation is absorbed by the closed volume due to multiple reflections. Thus for the radiative heat flow we obtain

$$Q_{21} = \sigma S (T_2^4 - T_1^4), \quad (1.11)$$

where S is the cross-sectional area of the orifice.

1.2.2 Thermal conductivity

The mechanisms of heat conduction in solids were already discussed in my bachelor thesis [4] and thus this section only briefly describes the notation necessary for calculations. Local heat flow density q is equal to the product of thermal conductivity $k(T)$ and the negative local temperature gradient. This relation is so called Fourier's law of heat conduction.

$$q = -k(T)\nabla T. \quad (1.12)$$

From Fourier's law we can derive the relation for heat flow in a simple case of a solid bar of constant cross-sectional area and with isotropic thermal conductivity

$$Q = \frac{S}{L} \int_{T_1}^{T_2} k(T) \, dT, \quad (1.13)$$

where S is the cross-sectional area, L is the length of the bar and T_1 and T_2 are temperatures at the ends of the bar.

As can be seen in Fig. 1.4, at low temperatures thermal conductivity has frequently very strong dependence on temperature. Integral thermal conductivity $K(T_1, T_2)$ is often used instead of $k(T)$

$$K(T_1, T_2) = \int_{T_1}^{T_2} k(T) \, dT. \quad (1.14)$$

Values of integral thermal conductivity for materials often used in cryogenics are tabulated [6]. An integral form of K is convenient, because it gives the possibility to determine values of K to any reference temperature

$$\int_{T_1}^{T_2} k(T) \, dT = \int_{T_0}^{T_2} k(T) \, dT - \int_{T_0}^{T_1} k(T) \, dT \quad (1.15a)$$

$$K(T_1, T_2) = K(T_0, T_2) - K(T_0, T_1) \quad (1.15b)$$

for $T_0 < T_1 < T_2$.

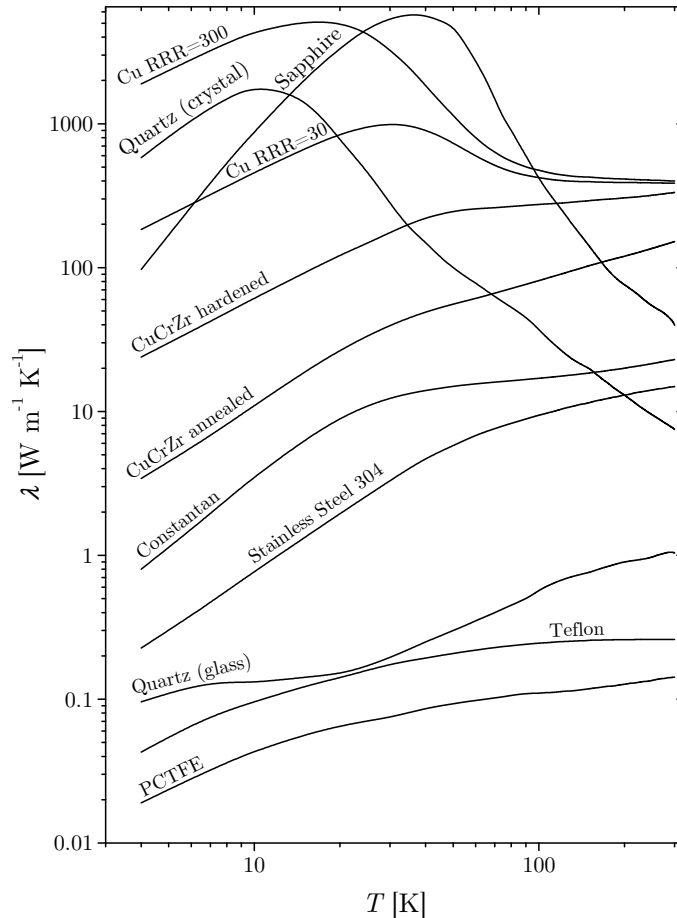


Fig. 1.4: Thermal conductivity of some common cryogenic materials. Data from [6, 12, 13].

1.3 Specific heat

To estimate the cooldown times or heating powers required for changing the temperature of the sample holder within certain time limit, the knowledge of heat capacity of used materials is essential. The heat capacity c is one of the most informative properties of material [7]. It is a measure of how much energy is needed to increase the temperature of a material. Specific heat at constant volume V of 1 mol of material is defined as

$$c_V = \left(\frac{\partial U}{\partial T} \right)_V = T \left(\frac{\partial S}{\partial T} \right)_V, \quad (1.16)$$

where U is the internal energy and S is the entropy of the system. Specific heat at constant pressure c_p is easier to estimate experimentally, but for solids and technical applications the difference between the two can be neglected. For estimation of the specific heat at room temperature, Dulong-Petit law can be derived considering lattice vibrations as classical harmonic oscillations along each degree of freedom.

$$c_V = \frac{\partial}{\partial T} (N_A 3k_B T) = 3k_B N_A = 3R, \quad (1.17)$$

where N_A is the Avogadro constant, k_B is the Boltzmann constant and R is so called universal gas constant. However, when the temperature of a material becomes close to or lower than Debye temperature Θ_D , one sees deviations from Dulong-Petit law and specific heat decreases with decreasing temperature. Debye temperature is defined as follows

$$\Theta_D = \frac{\hbar\omega_D}{k_B} \quad (1.18)$$

with \hbar as the reduced Planck constant. Θ_D thus proportional to maximum frequency of elastic oscillations ω_D . High value of Θ_D corresponds to strong interatomic forces (e.g. diamond) and vice versa [14]. Values of Debye temperature for a few elements and substances are listed in table 1.4.

Tab. 1.4: Values of Debye temperature Θ_D for some elements and substances. Data from [15].

	Diamond	Si	Al	Cu	NaCl	ZnS	Au	In	Pb
Θ_D [K]	1850	625	390	310	275	270	180	100	86

For derivation of specific heat relation at temperatures around or lower than Θ_D , one needs to approximate lattice vibrations by quantum harmonic oscillator potential and obtains

$${}^l c_V(T) = \frac{12\pi^4}{5} N_A k_B \left(\frac{T}{\Theta_D} \right)^3 \doteq 1944 \left(\frac{T}{\Theta_D} \right)^3. \quad (1.19)$$

This relation is valid for an insulator, where specific heat of electrons is negligible. This is not the case for metals. Using free-electron model one can derive electron increment to the specific heat

$${}^e c_V(T) = \frac{\pi^2}{2} N_A k_B \frac{T}{T_F} = \gamma T, \quad (1.20)$$

where γ is so called Sommerfeld constant and is, due to its dependence on Fermi temperature, material dependent. Generally, for any material specific heat is a sum of both lattice and electron increments

$$c_V = {}^l c_V + {}^e c_V = \beta T^3 + \gamma T. \quad (1.21)$$

Electron increment of specific heat of most of the metals is negligible for temperatures $T > 10^{-2}\Theta_D$, but around temperatures of liquid helium it might become dominant [6]. From equation (1.21) it is evident that this trend will be even stronger with further decreasing the temperature due to different exponents in temperature dependence.

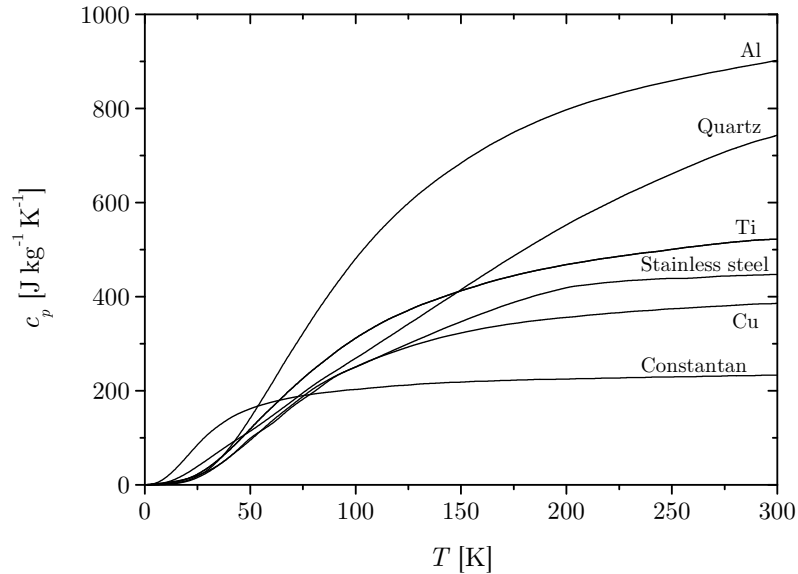


Fig. 1.5: Temperature dependence of the specific heat at constant pressure c_p for a few materials commonly used in cryogenics. Data from [12]

A number of further effects can contribute to the specific heat. Only single chemical element materials were discussed here and if more than one element is present, additional frequencies of oscillations are possible. Other effects that can lead to heat absorption are for example during order-disorder transitions or during heating over Curie temperature [16]. Heat capacities of some common cryogenic materials are shown in Fig. 1.5.

1.4 Thermal expansion

Thermal expansion process is described by the coefficient of thermal expansion, α , defined for one-directional case as

$$\alpha(T) = \frac{1}{l} \frac{\partial l}{\partial T} \quad (1.22)$$

with l as a length of a specimen.

To explain the effect of thermal expansion at low temperatures, one needs to consider the asymmetry of the potential between atoms. If this potential was quadratic, linear expansion would not exist. The potential between atoms can be approximated by the Lennard-Jones potential as a consequence of Pauli repulsion force and van der Waals attraction force, see Fig. 1.6. For excitations of atoms to low vibrational states that occur at low temperatures, the average position r_1 is near the classical equilibrium position at $T = 0$ K. At higher temperatures, higher excitations occur and the average position r_2 is at slightly larger interatomic distance. This corresponds to the thermal expansion effect. Hence, as the crystal is heated slightly above

absolute zero, negligible thermal expansion takes place. When the temperature is raised further, expansion begins, and its rate of increase rises.

Fig.1.7 shows the relative elongation $(L_T - L_{1K})/L_{1K}$ of a few materials. In gen-

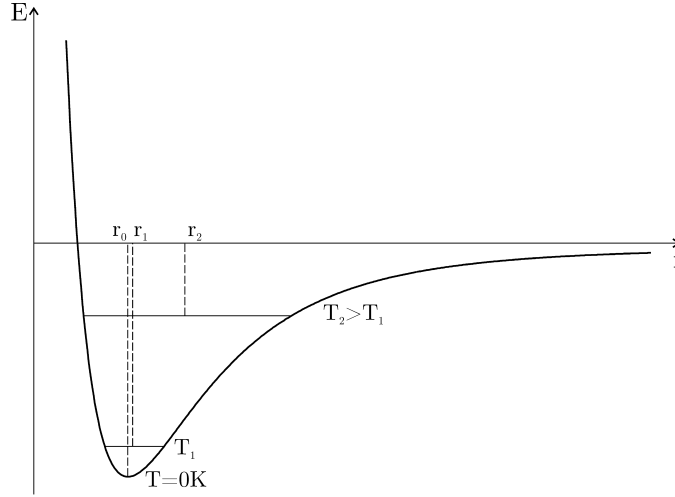


Fig. 1.6: Schematic representation of Lennard-Jones potential with average position of atom for three different temperatures $T = 0K, T_1$ and T_2 .

eral, metals contract by about 0.2-0.4 % and plastics around 1-2 % when cooled from temperature to low temperatures. From rather big differences in thermal contraction arises great care that needs to be taken when choosing materials in cryogenic design, especially when joining different materials. Luckily, most of the material contract substantially when cooled from room temperature to temperature of liquid nitrogen (77 K) and the contraction when cooling further is not significant. This fact makes testing the connections of two different materials, especially with glues and solders, very simple just by submersing connected parts to liquid nitrogen.

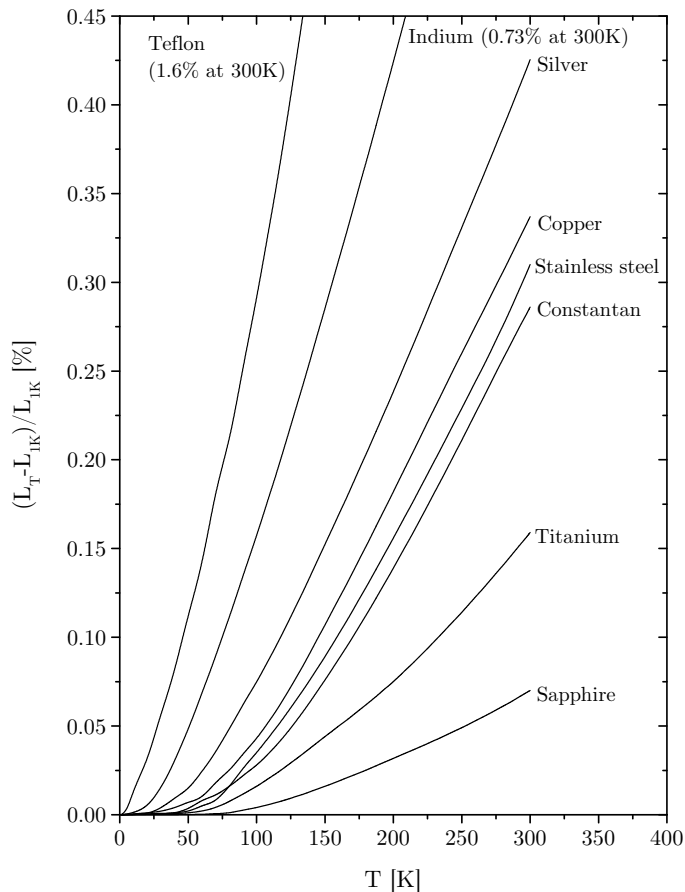


Fig. 1.7: Temperature dependence of relative thermal elongation $(L_T - L_{1K})/L_{1K}$ of a few materials. The ratio of length L_T at temperature T to the length L_{1K} at 1 K is plotted. Data from [12].

1.5 Mechanical properties at low temperatures

Mechanical properties such as yield and tensile strength, hardness or ductility are of key interest in low temperature design. Often necessity to reduce weight (e.g. to reduce cooldown time) or cross-sectional area (usually to reduce heat conduction) impose high demand on these properties.

Metals

In general, lowering the temperature of a solid will increase its strength and hardness, but lower its ductility. Young's modulus of elasticity does not vary much with temperature, but it typically increases in accordance with empirical law by $0.03\% \text{ K}^{-1}$ [6]. For purposes of cryogenics, normally the most widely used carbon steel is not applicable, due to its brittleness at low temperatures. However other metals such as aluminum, copper, nickel or most of their alloys including stainless steel do not exhibit this phenomenon. In the most cases, metals with face-centered

cubic unit cell do not become brittle while metals with body-centered cubic unit cell usually do [6].

Polymers

Plastics are used in cryogenics especially as distance elements when low thermal conductance is necessary. Most plastics at room temperature show flexibility (low Young's modulus) and high resistance to cracking, but when the temperature decreases this can change rapidly.

2 LT-STM PLATFORM WITH COOLED SAMPLE HOLDER

The LT-STM platform previously designed by J. Nekula [17] and inspired by commercial variable temperature STM [2] was redone to the state shown in Fig. 2.1. Inside the UHV chamber on the table insulated from vibration by spring and electromagnetic damping there is a STM scanning head at room temperature and a sample holder that can reach cryogenic temperatures. Sample holder is thermally insulated from the table via low conductive supports discussed in chapter 4. Since the scanning head and the sample holder are not mounted together as one body but placed separately on the table, the rigidity of the setup is lowered. To avoid tip-to-sample vibrations, both the scanning head and the sample holder must be stiffly mounted to the table. Thus the supports were specially designed for insulating of the sample holder with high mechanical stiffness. The sample holder is also shielded against room temperature radiation by a shield placed around it. Both the sample holder and the radiation shield are cooled by the cryogenic helium flow cooling system with two heat exchangers. The thermal connection of cooled parts and heat exchangers is realized by multiple fine high conductive copper wires, so called braids. Sample holder is connected to the first heat exchanger and the radiation shield to the second heat exchanger using warmed up helium from the first one.

For the described setup the total maximum heat load on the first heat exchanger Q_M was estimated not to exceed 0.5 W and Q_S not to exceed 1 W. For the lowest temperature of the sample holder (with mass less than 50 g) of 20 K, the temperature of the first heat exchanger T_{V1} around 5 K is needed, because of the temperature drop on the braid. With the lowest expected temperature difference of the incoming and outgoing helium in exchangers to be 5 K and 10 K respectively, the required mass flow rate \dot{m} was estimated. Knowing the necessary mass flow rate, the flow cooling system discussed in the next chapter 3 was designed.

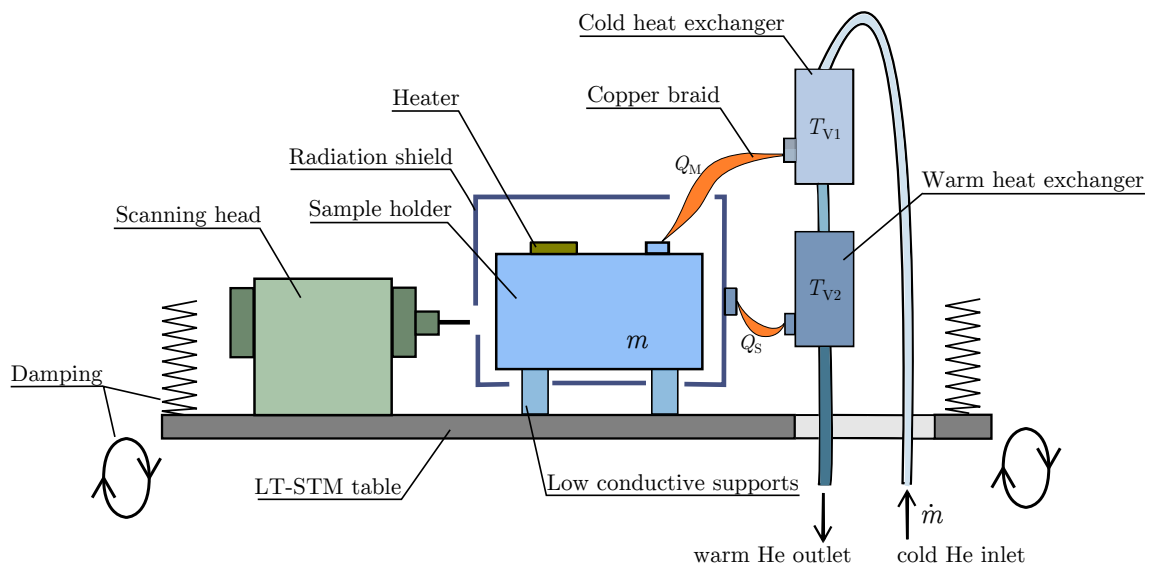


Fig. 2.1: The scheme of the STM platform with the cooled sample holder and the scanning head at 300 K.

3 FLOW COOLING SYSTEM

Based on the requirements of the Scanning probe microscopy group at the Institute of Physical Engineering (IPE), the flow cooling system shown in Fig. 3.1 was designed. Its principle is as follows: liquid helium from pressurized external Dewar vessel flows through the transfer line with one end inserted in the vessel submersed into liquid helium and other end inserted into the inlet of the flow cryostat. Here helium enters a thin capillary and is transferred to heat exchangers. There are two heat exchangers connected in series. The first heat exchanger on lower temperature is thermally connected to the sample holder while the second warmer heat exchanger is thermally connected with radiation shield around the sample holder. Warmed up helium gas that leaves heat exchangers exits the system via thin-walled tube. Relatively low temperature of the leaving gas is used to cool a radiation shield around the inlet of the cryostat. Dewar vessel is pressurized by its own vaporization and additional pressure can be applied from a pressure bottle with helium gas at room temperature.

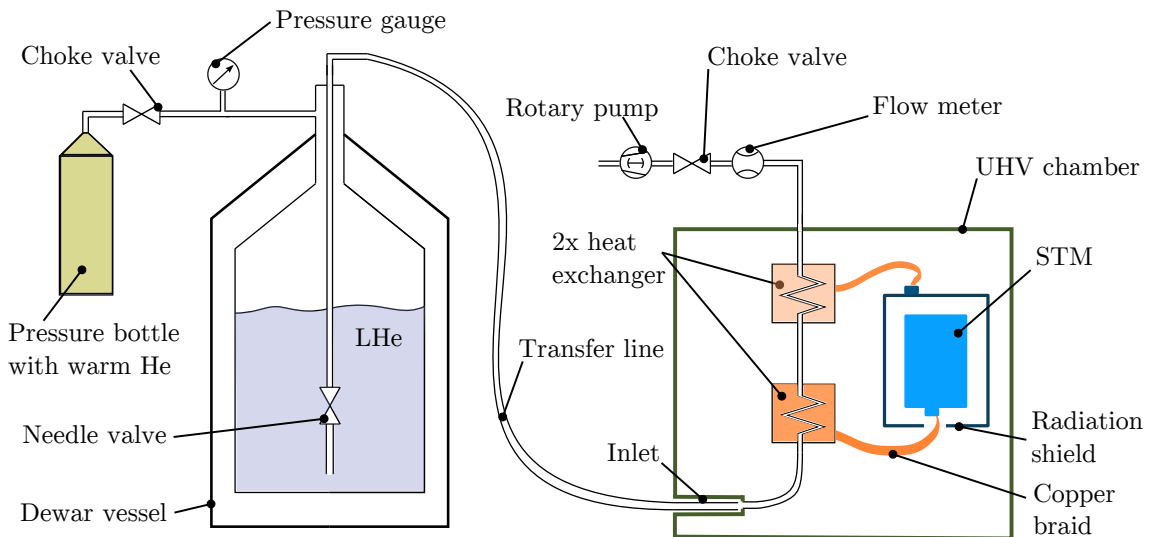


Fig. 3.1: The scheme showing the principle of the flow cooling.

The flow rate is regulated by valves on the pressure bottle and on the outlet of the cryostat. When desired, additional pressure drop can be increased with the rotary pump and regulated with the outlet choke valve. In case of a new transfer line, that will be mentioned later, there is also a needle valve at the end of a transfer line submersed in liquid helium inside the Dewar.

The flow cryostat is designed as a portable cooling device that can be mounted to any vacuum chamber with a CF40 flange. Inside the chamber one only needs to connect the cooled device with heat exchangers by a stranded wire made of highly conductive copper, so called braid.

3.1 Helium inlet and outlet

Fig. 3.2 shows the section view of the helium inlet and outlet assembly. Note that the heat exchangers are not displayed in this view as a special section 3.2 is devoted to their design. The entire cryostat has elongated T-shape and is about 400 mm long and 170 mm high. The outer shell tube is 40 mm in diameter and the requirement for its length comes from the temperature gradient from room to helium temperature on the inlet stainless steel tube inside it, see section 3.1.1. The removable helium transfer line is terminated with a connecting piece made of PTFE G405 machinable plastic¹. It is a standard polytetrafluorethylen (PTFE) reinforced by 25 % of glass. The material shows good machinability, ductility and vacuum compatibility. A leakless fit between this piece and the stainless steel capillary terminal is secured, as PTFE is relatively soft material and it adopts oneself to the terminal. Moreover, the thermal contraction of PTFE is higher than that of stainless steel (Fig. 1.7) and thus the fit is even tighter when cooled down. When the transfer line is fitted in place, its position is locked with the tightening ring that presses a rubber O-ring around the tube. When the position is locked, a closed space between the transfer line and a stainless steel tube is created possibly with some amount of liquid helium. As mentioned in theoretical section, when helium evaporates, it expands and the overpressure could destroy the apparatus. Thus a simple safety relief valve is mounted on the seal of the cryostat (only the screw hole is shown in Fig. 3.2).

The stainless steel inlet tube needs to be thin walled to reduce heat losses and its mechanical stiffness is thus limited. To protect the tube against bending, 6 distance elements are placed around it perpendicular to the outside wall. The distance elements are 0.5 mm far from the sidewall when the tube is coaxial. Some distant elements might touch the sidewall, so their tips are sharpened to reduce the contact surface and thus thermal conductance. Polymer Techtron[®] HPV was used for the distance elements due to its low thermal conductivity and ultra high vacuum compatibility.

¹Acquired from Tribon Ltd., Stará Boleslav.

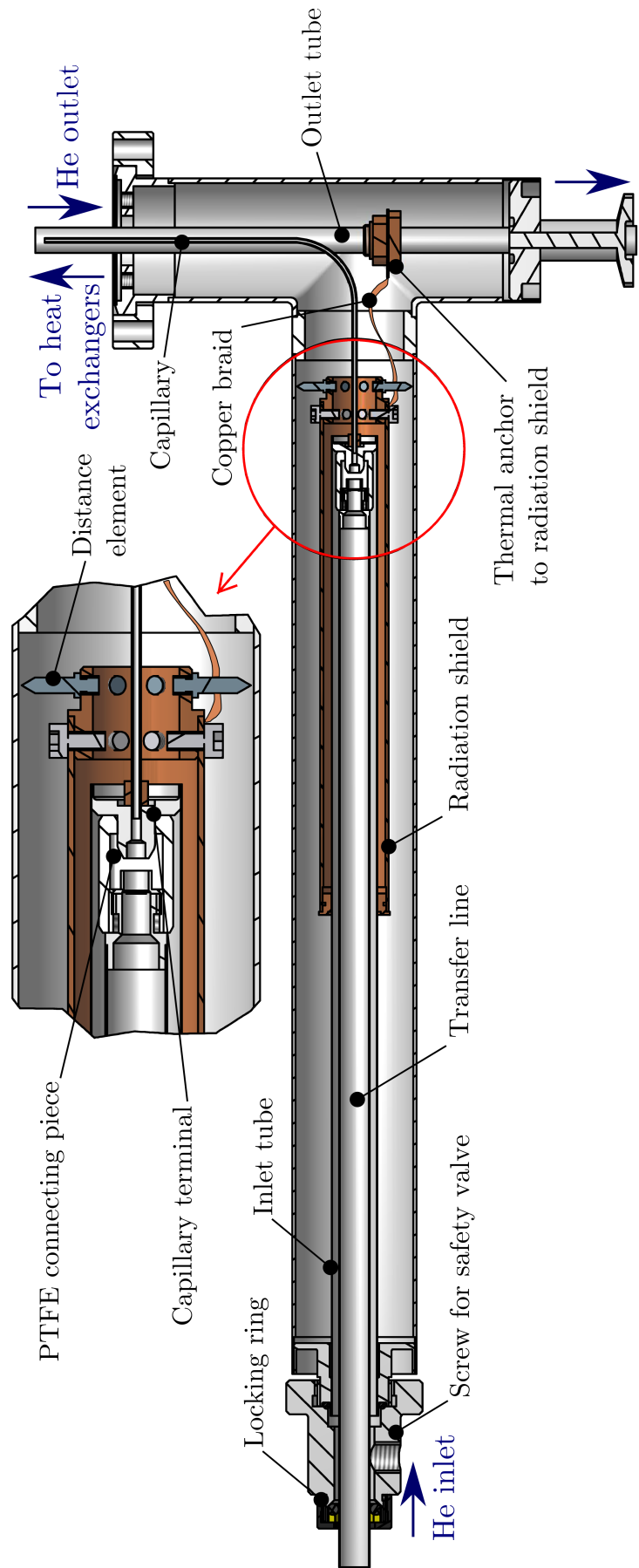


Fig. 3.2: The flow cryostat without heat exchangers. A part of the helium transfer line is also shown in a position during operation.

3.1.1 Inlet tube calculation

To present preliminary a calculations conducted prior to the final design, the estimation of an optimal length of radiation shield around helium inlet is presented here. As discussed in theoretical section, all parts at liquid helium temperatures must be shielded against room temperature radiation in order to minimize heat losses. It is very advantageous to use the cold helium gas leaving the cryostat for this purpose. Thus a copper tube thermally connected on one end to the outlet stainless steel tube via copper braid is utilized as a radiation shield, see Fig. 3.2. The other end of the shield is attached to the stainless steel inlet tube. Thus the helium outlet serves as a thermal anchor that drains partially the heat flow conducted by the inlet tube from its room temperature end.

The purpose of the calculation is to estimate the proper length of the shield. Scheme on Fig. 3.3 shows the model used for the calculation with all considered heat flows. In this model the inlet tube and the transfer line are replaced by a single tube with such wall thickness that it has a cross-sectional area of both tubes together. The left side of stainless steel inlet tube is mounted at room temperature while the right end is at the temperature of liquid helium coming from the transfer line. The tube is 300 mm in length with outer diameter of 14.4 mm and wall thickness of 0.35 mm. At position l , the radiation shield is connected. As an input of the calculation, it is necessary to estimate the heat flow through the braid and the temperature at which it connects to the radiation shield. Based on the thermal considerations in heat exchangers, which will be discussed later, the values were set as $Q_B=325$ mW and $T_S = 160$ K and the thermal conductivity was of the braid was used from the previous measurements [4].

When the radiation shield is too long, it collects too much radiative and conductive heat flows which cannot be drained away by the braid. The shield warms up and flows Q_{RST} and Q_{ST} to the capillary terminal increase. On the other hand, when the shield is too short, the radiation to the unshielded part Q_{RT} is too high.

The problem was modeled in COMSOL MultiphysicsTM and the calculated temperature profiles are shown in Fig. 3.4. The solution was found for $l = 150$ mm. For this length the calculated heat flow Q_B drained by braid to keep the temperature at the right end of the shield at 160 K is 315 mW. Due to very high thermal conductivity of copper, the temperature at the other end of the shield is only 1.3 K higher. Resulting heat flow to the helium capillary terminal is 51 mW. If there was no shield present, expected heat flow would be 196 mW.

The verifying calculation with less complex program KRYOM [18] was also performed. In this program the whole complex problem can not be simulated, but partial heat flows can be verified. Using a few simplifying assumptions, such as

isothermality of radiation shield, heat flow to the helium inlet was estimated as 68 mW. The result is in agreement with COMSOL model within 25 %.

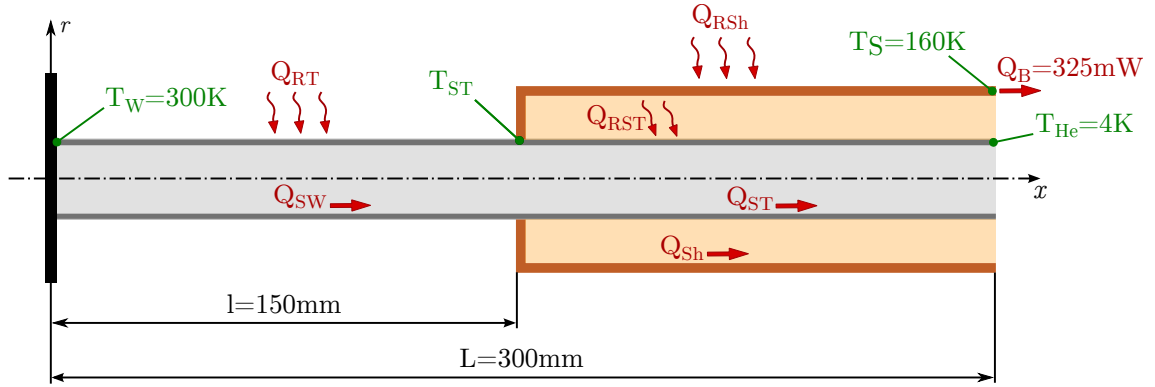


Fig. 3.3: Input tube heat calculation scheme. All heat flows taken into account are shown.

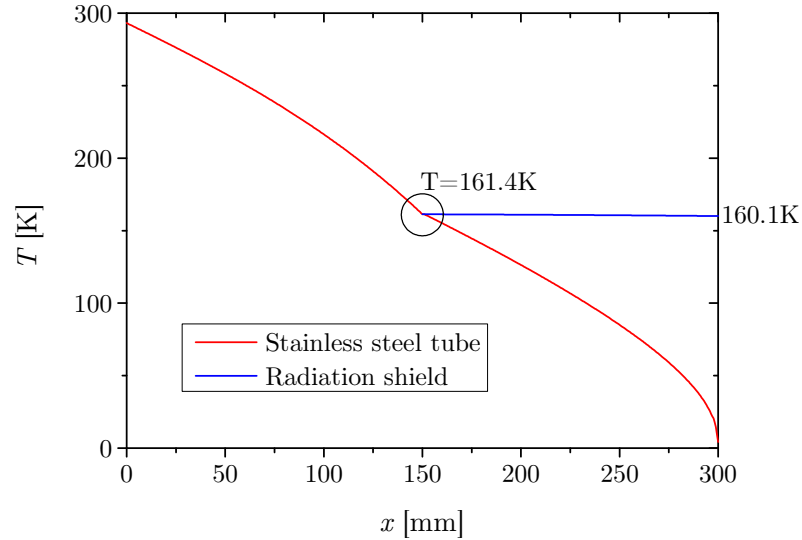


Fig. 3.4: Temperature profiles calculated with Comsol Multiphysics.

3.1.2 Anchoring the braid on output tube

When Fig. 3.2 is studied carefully, one can ask how the braid was connected to the outlet tube and radiation shield. The braid needs to be mounted after the inlet tube with radiation shield and the output tube are at their places. Then the only access to the inside of the cryostat is through the top opening - the connection to the vacuum chamber. Simple soldering on the spot does not come into consideration as there is not enough room to operate.

A solution is shown in Fig. 3.5. Before inserting the radiation shield inside the T-tube, one end of the braid is connected to the radiation shield. A small copper

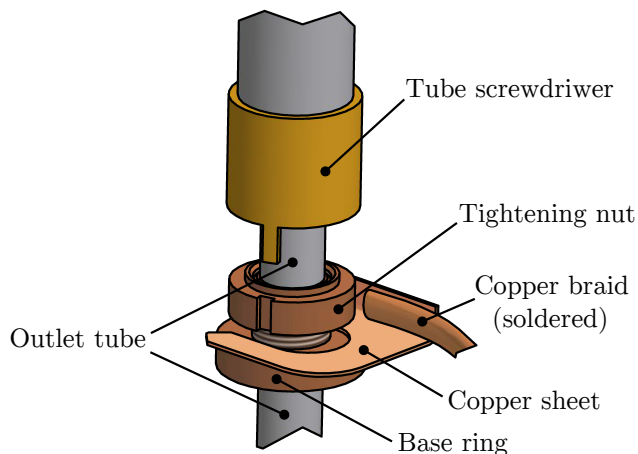


Fig. 3.5: The design of the anchor of the braid on the output tube.

sheet is soldered to the other end. The copper sheet has a U-shape fitting onto a copper base ring on the stainless steel output tube. During assembly, the sheet is carefully placed using tweezers on top of the base ring and secured with the copper ring with a screw. The ring is screwed with a special tube screwdriver which is also shown in Fig. 3.5. The screwdriver can be used, because the heat exchangers are not yet mounted on the output tube and nothing blocks putting another tube around the output tube from the top.

The installation of the capillary is not such a big problem, because of its flexibility. Before inserting, it is preshaped at the length of the bending and fine shaped from the top opening. The contact with the sidewall must be avoided, since it would create a significant parasitic heat flow and heat up the helium on its way to the heat exchangers.

3.2 Heat exchangers

3.2.1 Assembly

There are two identical heat exchangers coupled in series, see Fig. 3.6. Helium from thin-walled capillary enters the first heat exchanger thermally connected with the sample holder via a copper braid. After it warms up it continues to the second heat exchanger cooling the radiation shield around the sample holder. Both heat exchangers are surrounded by a copper tube acting as a radiation shield, thermally connected to the second heat exchanger. This ensures that radiation from surroundings only elevates the second heat exchanger's temperature while the first heat exchanger, which lowest achievable temperature is important, is shielded.

Thermal connection of the heat exchangers is realized by thin-walled stainless steel tube only 16 mm in length. Even though the tube is short, it does not transfer significant heat flow to the colder heat exchanger, because it is cooled by cold helium that flows inside it.

There are two heaters and three thermometers placed inside the assembly. The first thermometer measures the temperature of the inlet capillary which corresponds to the temperature of helium prior to entering the first heat exchanger. Then there is one thermometer on each of the heat exchangers. For applying the heat loads during testing and also to regulate the temperature of the heat exchangers more finely than by regulating the flow rate of helium, there is also a heater on each of the heat exchangers. The heaters consist of simple 2 k Ω SMD resistors.

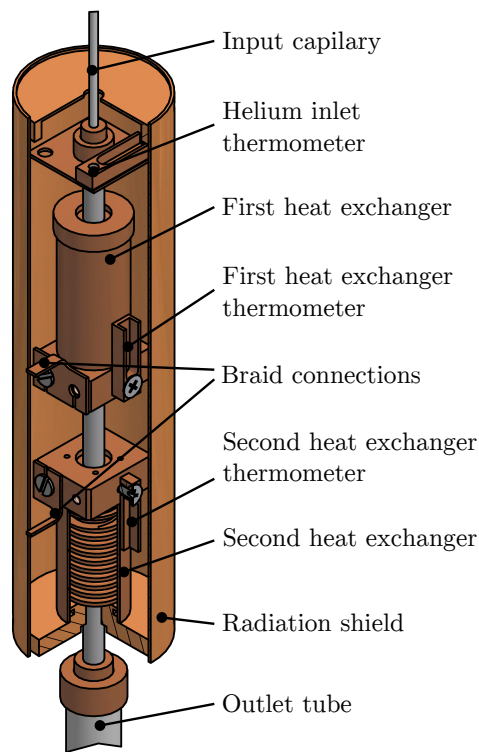


Fig. 3.6: The section view of the heat exchanger assembly.



Fig. 3.7: Three main parts of the heat exchanger: the main body with the helical groove, the copper tube that covers the groove around it and the closing cap to connect the tubing.

3.2.2 Calculations

The heat exchanger is basically a copper cylinder with helical groove in which the helium is forced to flow, see Fig. 3.7. The groove creates sufficient heat exchange surface area where the heat can be absorbed by the fluid. To ensure good efficiency of the heat exchangers, some flow calculations needed to be carried out prior to the design.

The heat exchange efficiency is higher when the flow is turbulent inside the groove. In order to achieve the turbulent flow, the speed of the flow needs to be sufficiently high and thus the cross-sectional area of the groove sufficiently small. On the other hand, with decreasing cross-sectional area the pressure drop increases while the Dewar vessel has an operation pressure limit of only 0.6 bar and one needs to find a compromise. The process of calculation is not straightforward since the values of many variables are unknown and one often needs to use estimations.

Maximum transferable heat estimation

First of all, it is necessary to estimate the heat load Q on each of the heat exchangers for various temperatures of the sample holder and radiative shield. This calculation will follow in chapter 5. Once the heat load is known, then the mass flow rate \dot{m} can be estimated using simple equation

$$Q = \dot{m}c_p (T_{VA} - T_{VB}), \quad (3.1)$$

where T_{VA} and T_{VB} are the temperatures of helium gas entering and leaving the heat exchanger and c_p is the specific heat of helium. Note that c_p is considered constant, which is reasonable for small temperature differences. We assume that all liquid

helium evaporates in the transfer line and only helium gas at about 5 K enters the heat exchanger. One also needs to assume certain temperature drop on the heat exchanger.

Knowing the mass flow rate, the speed of the gas u_d and Reynolds number Re in the groove can be calculated

$$u_d = \frac{4}{\pi d^2} \frac{\dot{m}}{\rho}, \quad (3.2)$$

$$Re = \frac{u_d d}{\nu_{\text{kin}}} = \frac{4\dot{m}}{\pi\eta d}, \quad (3.3)$$

where d is the diameter of the groove, ν_{kin} and η are kinematic and dynamic viscosities of helium gas and ρ the density of helium gas. Using Reynolds number and tabulated Prandtl number Pr , the effectiveness of the heat exchange can be estimated. It is described by another dimensionless parameter - Nusselt number Nu

$$Nu = 0.023 Re^{4/5} Pr^{2/5}. \quad (3.4)$$

This is the Dittus-Boelter correlation and is only valid for the turbulent flow [19]. Finally, now the heat transfer coefficient α_h can be calculated and used to estimate the maximum transferable heat flow from gas to walls of the groove Q_{max}

$$\alpha_h = \frac{Nu k}{d}, \quad (3.5)$$

$$Q_{\text{max}} = \alpha_h S \Delta T_v. \quad (3.6)$$

Here S is the cross-sectional area and ΔT_v is the temperature difference between the mean temperature of the helium gas and the temperature of the heat exchanger. It is important to distinguish between Q_{max} and Q from equation (3.1). The first one tells the maximum amount of heat that can be drained by heat exchanger. It does not take into account the heat capacity of the fluid, for that there is Q . In order to have an efficient heat exchanger, a condition

$$Q_{\text{max}} \geq Q \quad (3.7)$$

should be valid for any flow rate and temperature.

Pressure drop estimation

When the groove is designed in such a way that condition (3.7) is valid, it is still important to check if the groove, or any other part of the helium line, does not create too high pressure drop. There are two types of pressure losses: Δp_z caused

by the changes of diameter of the tubing and the pressure loss caused by friction of the gas Δp_t . Δp_z is defined as follows

$$\Delta p_z = \xi \frac{u_d^2}{2} \rho, \quad (3.8)$$

where ξ is the loss coefficient. The values of ξ are tabulated for various tubing cross-section area ratios and can be found for example in [20]. The friction pressure drop Δp_t is defined as

$$\Delta p_t = \lambda_t \frac{L}{d} \frac{u_d^2}{2} \rho, \quad (3.9)$$

where L is the length on which is the pressure loss calculated and λ_t is the friction coefficient. For the laminar flow, the expression $\lambda_t = 64/Re$ is used. In case of the turbulent flow, λ_t is a function of Re and the groove wall roughness. Its value can be found using Nikuradse diagram, found for example in [20].

The two identical heat exchangers were designed with respect to the results of the calculations and some of its parameters can be seen in Tab. 3.1 below. The final mechanical design was carried out by P. Hanzelka.

Tab. 3.1: Basic parameters of the heat exchangers.

Diameter of the helix	9.5 mm
Pitch of the helix	1.5 mm
Length of the helix	300 mm
Cross-sectional area of the groove	0.75 mm ²
Total heat exchange area	900 mm ²
Maximum cooling power ¹	0.5 W
Reynolds number ¹	5.00×10^3
Pressure drop with 300 K He gas ²	15 kPa
Pressure drop with 5 K He gas ²	0.6 kPa

¹for 0.31/h of LHe and boundary temperatures 4.2 and 20 K.

²for 0.31/h (8×10^{-6} kg/s) of LHe.

3.3 Testing vacuum chamber

For quick tests at the ISI, a vacuum chamber was designed and manufactured, see Fig. 3.8. It was designed as a small multipurpose cell primarily for testing of the STM cooling, but allowing different experimental setups in the future.

The chamber is a simple cylinder 220 mm in diameter and 280 mm high. The size was chosen so that the whole STM setup could fit in including the damping

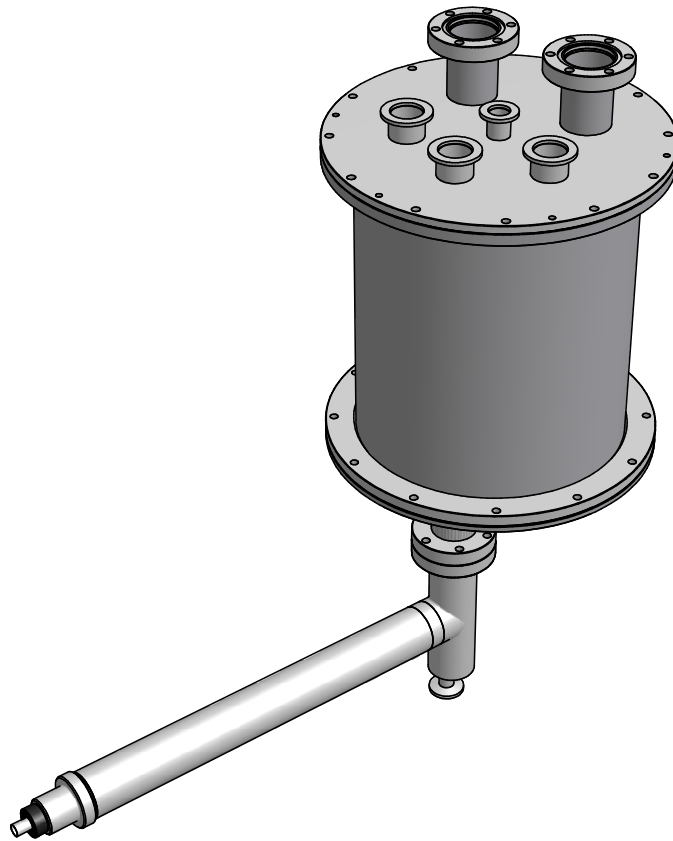


Fig. 3.8: Testing vacuum chamber with the flow cryostat connected to the bottom flange.

(using the current STM working at room temperature described in diploma thesis of J. Nekula [17]). There are two CF40 vacuum flanges to copy the existing UHV chamber at the IPE, in which the STM is operating. Three KF25 flanges are also placed at the bottom used mostly for the electrical feedthroughs. The same types of the flanges are placed on top of the chamber as well, but positioned differently. There is also a small KF16 flange both at the bottom and the top of the chamber on its rotation axis in the middle for potential low temperature material characteristics measurements.

3.4 Tests of the cooling system

3.4.1 Pressure drop measurement

From the table 3.1 it is evident that the pressure drop will be the highest at the beginning of the cooldown when the flowing helium gas is at room temperature and has the lowest density. Therefore the first and easiest test to be carried out was to verify the calculated pressure drop on the new flow cryostat. A pressure bottle with

room temperature pressurized helium and regulation needle valve was connected to the input system and the flow rate was measured with a precise wet drum flowmeter on the output. The results can be seen in Fig. 3.9 together with calculated values for two extreme conditions considering both laminar and turbulent flow in the whole setup using adequate coefficients λ_t from equation (3.9) for the two cases. Measured data sits in between the two, because different type of flow is expected in different sections of the tubing.

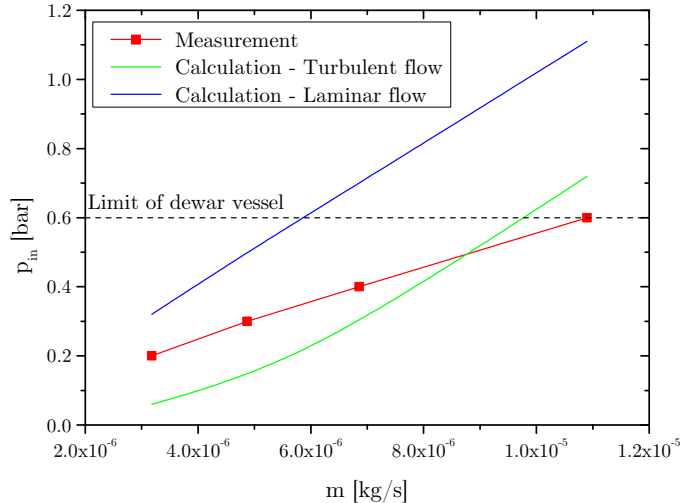


Fig. 3.9: Pressure loss measurement with room temperature helium gas. The calculated dependence of the pressure in the Dewar on the mass flow rate in the cryostat is compared with the experiment. Two calculation models are shown. One assumes the laminar flow in the entire cryostat (blue triangles) and the other assumes the flow to be turbulent (green circles). The measured values (red squares) sits in between the two in the region of the values permissible by the safety limit of the Dewar vessel.

3.4.2 First cooldowns

The goal of the first experiments was to measure the time needed to cool down the heat exchangers to a stable cryogenic temperature, to estimate the LHe consumption of the cryostat and to test the general performance of the flow cryostat under various conditions. When desired, the heat load could be simulated with the heaters attached to both of the heat exchangers. There were three temperatures measured: T_1 on the capillary right before entering the first heat exchanger and the temperatures T_2 and T_3 of the first and the second heat exchanger respectively. In this experiment helium throughput was measured with standard diaphragm gas flow meter instead of the more precise wet drum flow meter due to higher mass flows and more convenient measurement.

The time to cool down both heat exchangers without any heat load applied to them was measured to be around one hour. The cryostat proved its functionality and the lowest temperature of 11 K was reached. However, the low temperatures could be reached only with unacceptably high LHe consumption, see Tab. 3.2. Moreover, the unwanted effect of temperature oscillations was observed in the flow cryostat. The oscillations were probably caused by the helium evaporation. When helium evaporates, the pressure locally significantly increases. This local increase of pressure prevents constant flow of helium through the heat exchangers and they warm up. After a few seconds the liquid helium overcomes the pressurized vapor, gets to the heat exchangers, lowers their temperature and the whole process repeats.

Tab. 3.2: Cryostat with the old version of the transfer line. Typical measured values of temperatures of helium before entering first heat exchanger T_1 , of the first and second heat exchanger T_2 and T_3 together with the throughput and additional heating on the first heat exchanger.

T_1 [K]	T_2 [K]	T_3 [K]	Throughput GHe (300 K), [l/s]	Consumption LHe (4.2 K), [l/h]	Heating [mW]
11.2	11.0	11.2	0.722	3.71	0
23.2	23.9	24.9	0.309	1.59	200
25.7	27.2	28.5	0.275	1.42	392
43.2	43.1	44.3	0.147	0.76	0

Very high helium consumption was caused by the inappropriate helium transfer line. This can be seen most apparently in the first line of the table 3.2. There, even for a huge LHe consumption of more than 3.5 l/h the temperature of the helium entering the heat exchangers did not get lower than 11 K. For the described experiments, we used the helium transfer line than was not optimal for the use together with the flow cryostat. It was designed for the refilling of liquid helium for the sorption cryopump [21]. Since this transfer line is only meant to use for short periods of time during refilling, some losses due to parasitic heat flows are acceptable. However, in case of the flow cryostat helium flows continuously with much smaller flow rates and there is enough time for it to warm up before it gets to the heat exchangers.

P. Hanzelka designed a new low-loss transfer line specially for the use with the flow cryostat with total parasitic heat loss of less than 900 mW. Moreover, the new transfer line includes a small needle valve at the end that is inserted into the Dewar vessel. The valve can be regulated from the outside even during the operation. We believed that the regulation of the flow already at the inside the Dewar will

significantly lower the thermal oscillations in the system.

3.4.3 Test with the new transfer line

By the time the new transfer line was finished, a dummy sample holder, which will be discussed in detail in the next chapter, was already installed in the testing vacuum chamber. A mass that serves as a model of the cooled sample holder was thermally connected to the first heat exchanger via copper braid and its temperature T_4 was also measured. Thus there is always a heat load of about 200 mW present at the first heat exchanger (caused by radiation on the model and by conduction via its insulation). Only the results of the measurements that are related to the flow cryostat are discussed in this section while the rest concerning the dummy will be mentioned in the next chapter.

The new low-loss transfer line significantly decreased the amount of liquid helium needed to get the heat exchangers to low temperature. For the illustration, the temperature $T_1 = 4.4$ K was reached with consumption of 1.8 l/h while with the old transfer line $T_1 = 11.2$ K was reached with twice as high consumption. Moreover, the cooldown time of heat exchangers decreased to about half from one hour to 30 minutes. Tab. 3.3 below shows some typical values of temperatures and the corresponding LHe consumptions reached using the new transfer line.

Tab. 3.3: Cryostat with the new transfer line. Typical measured values of temperatures of helium before entering first heat exchanger T_1 , of the first and second heat exchanger T_2 and T_3 together with the throughput and additional heat load on the first heat exchanger. See how the LHe consumption decreased compared with Tab. 3.2, also note the lowest temperature achieved is close to 4.2 K this time.

T_1 [K]	T_2 [K]	T_3 [K]	Throughput GHe (300 K), [l/s]	Consumption LHe (4.2 K), [l/h]	Heat load [mW]
4.4	4.5	4.5	0.36	1.86	200
9.8	13.9	16.6	0.14	0.73	200
21.7	31.6	40.3	0.06	0.32	200
29.3	42.4	53.5	0.04	0.22	200

4 FOUR BALL SUPPORTS

To insulate the sample holder from the parts at room temperature, the low conductive supports with glass balls were designed and realized. The design of these four ball supports (FBS) was already discussed in my bachelor thesis [4]. Nevertheless, a chapter is devoted to them in this masters thesis as well, since they were studied further. Specifically, attention was focused on the description of heat flow through the spot contact between the balls. The FBS were also utilized as a thermal insulation of the model of the sample holder and the setup was experimentally tested. The experiment to roughly estimate the mechanical stiffness of the support was also carried out.

4.1 Description of the support

The temperature difference between the cooled sample holder and parts at room temperature will be over 250 K and therefore substantial thermal insulation is important. On the other hand, it is important to ensure high mechanical stiffness of the mount. These two requirements contradict each other and a compromise needs to be found.

The support consists of four borosilicate glass balls of 2.5 mm in diameter forming a tetrahedron, see Fig. 4.1. The presumption is that, due to high mechanical stiffness of the balls, there is only a small contact area between the balls resulting in low heat conductance of the support.

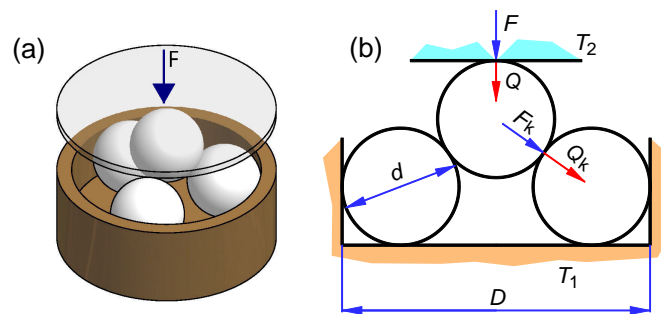


Fig. 4.1: (a) Principle of the support. (b) Bent section view showing contacts between the balls and top ball with the metallic plate. The contact resistances between the balls and bottom plate are neglected.

4.2 Spot contact

The thermal resistance of the support is determined by partial resistances of the spot contacts. There are three different types of contact in the support. First the metallic plate with the top ball, then the contacts between the top ball and three bottom balls and finally contacts of the bottom balls with the metallic seat (see Fig. 4.1 b). We assume that the thermal resistance of the third type is negligible, because each of the bottom balls is in contact with the bottom seat twice (and one of the contacts is even convex-to-concave) [4]. The two first types of the spot contact were studied.

The first step of the heat flow calculation is the estimation of the contact surface area using simple Hertz equations, already described in my bachelor thesis [4]. The radius of the calculated contact surface did not exceed 0.1 mm assuming the highest loading force of 10 N. The ball's radius is 1.25 mm, thus the curvature of the ball close to the contact area can be neglected. Once the contact area is known, the heat flow through the contact can be calculated.

4.2.1 The simplest model

First, we used a simple model derived by V. Musilová using Fourier law of conduction shown in Fig. 4.2.

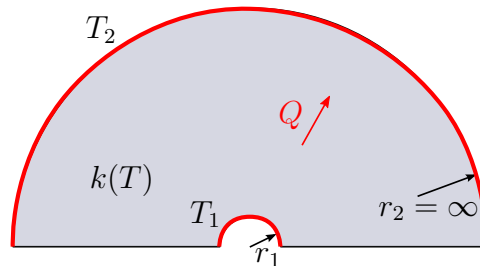


Fig. 4.2: The first model for calculation of heat flow through a spot contact. Constant temperature T_1 of the hemispherical area around the spot contact with radius r_1 is assumed.

The model calculates the heat flow Q from the half sphere with the radius equal to the spot contact radius r_1 to the half sphere with infinite radius r_2

$$Q = 2\pi r_1 [K(T_1, T_2)], \quad (4.1)$$

where $K(T_1, T_2)$ is an integral thermal conductivity described in section 1.2.2, because the temperature dependence of thermal conductivity needs to be taken into account. This model gives a reasonable insight into how much heat is transferred from a spot contact to a half space, however it is still quite far from reality. Especially

because it assumes that the whole half sphere with radius r_1 around the spot contact is isothermal. Naturally, this simplification is hard to justify, because the biggest thermal resistance occurs right near the contact area.

4.2.2 Numerical model

The problem of a spot contact was studied further using numerical methods by commercially available software COMSOL Multiphysics. The model presented in Fig. 4.3 was applied. The half spaces are approximated by two half spheres separated by a small gap and connected in the middle with a circular contact of size calculated from Hertz equations.

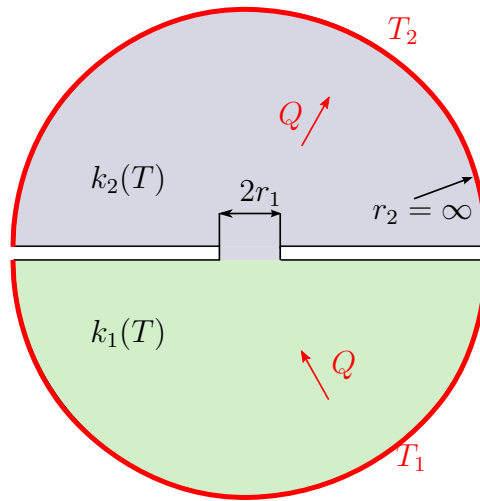


Fig. 4.3: Scheme showing geometry of the numerical calculation and the boundary conditions.

Fig. 4.4 shows the actual numerical model. Only one side of the half spaces is shown due to rotational symmetry of the problem. The choice of the proper mesh construction and density proved to be the main problem. In order to have a well defined mesh, there needs to be a tiny half sphere in the middle of the spot contact (see Fig. 4.4 c). However, this defect can be very small and at the used size being about 25 times smaller than the contact surface diameter. It does not play significant role on the resulting heat flow. The reasonable results were only obtained with a mesh consisting of concentric circular sectors with strongly variable density at places with expected high temperature gradient.

Fig. 4.5 shows the temperature distributions for the contact with metallic plate and for the two balls mutually. As expected, the thermal conductivity of aluminum is much higher and in the glass-metal contact the temperature gradient occurs only in the glass material. More importantly, the study confirmed the assumption of isothermal ball-ball contact as it can be seen in Fig 4.6 which shows the temperature

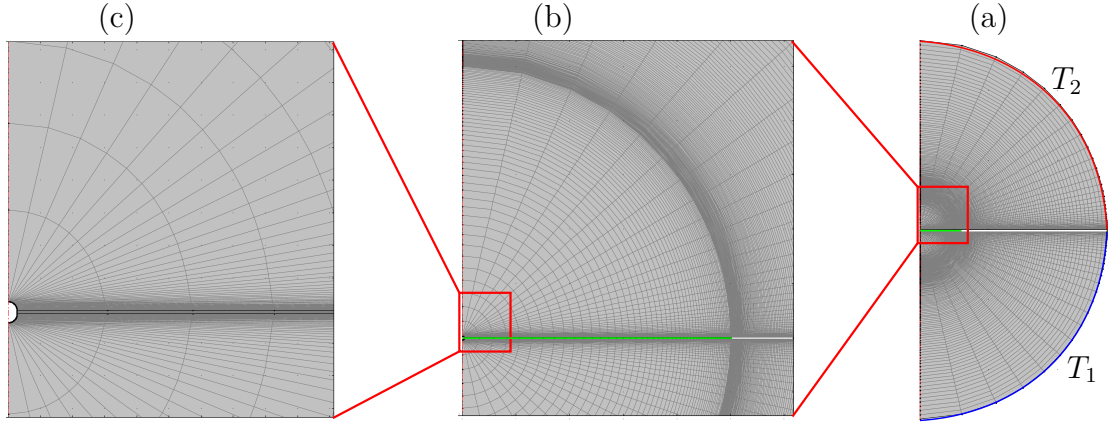


Fig. 4.4: The meshed model for the numerical calculation of the heat flow through the spot contact. (a) The whole calculation area. Temperature boundary conditions (blue and red) and the conducting spot contact area (green) are highlighted. (b) Detail of the calculation area around the spot contact. Strong nonlinearity of the mesh is clearly visible. (c) Detail of the half sphere defect needed for proper concentric meshing.

distribution of the ball-ball contact area. A steep slope of the curve in the middle is caused by the earlier mentioned mesh defect. Except for the region around it, the isothermality of the contact was found within 0.3 K. Note that temperature of the contact T_c is not the mean of T_1 and T_2 . Due to the same materials in both half spaces, the heat flows in both of them must be the same as well. Therefore, we obtain the condition

$$K(T_1, T_c) = K(T_c, T_2). \quad (4.2)$$

Since the thermal conductivity is not constant, T_c is not the mean of T_1 and T_2 . From this condition we find the $T_c = 199.0$ K while the value obtained from the numerical model is 196.5 K, see Fig 4.6, which is in a good agreement within 1.5 %.

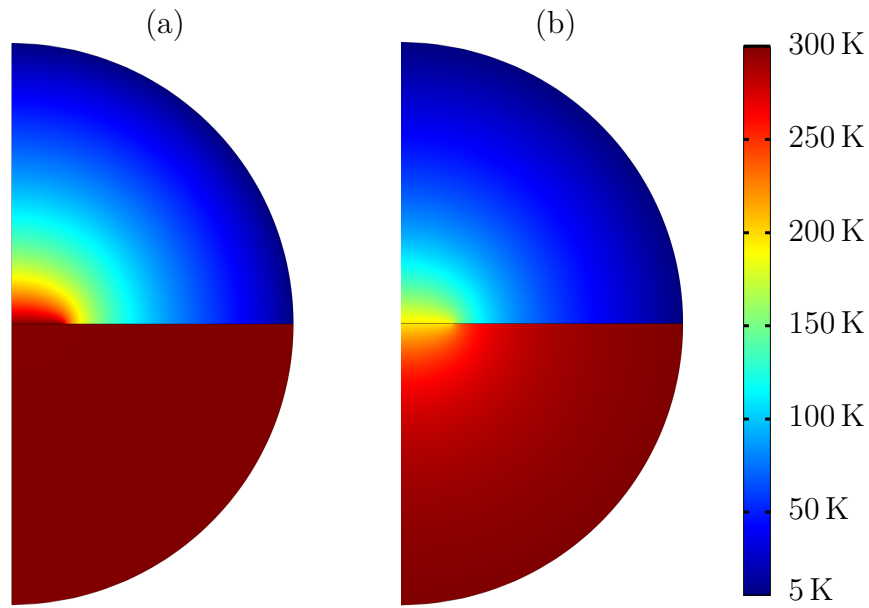


Fig. 4.5: Calculated temperature distributions around the spot contact for the (a) metal-to-glass contact (b) glass-to-glass contact.

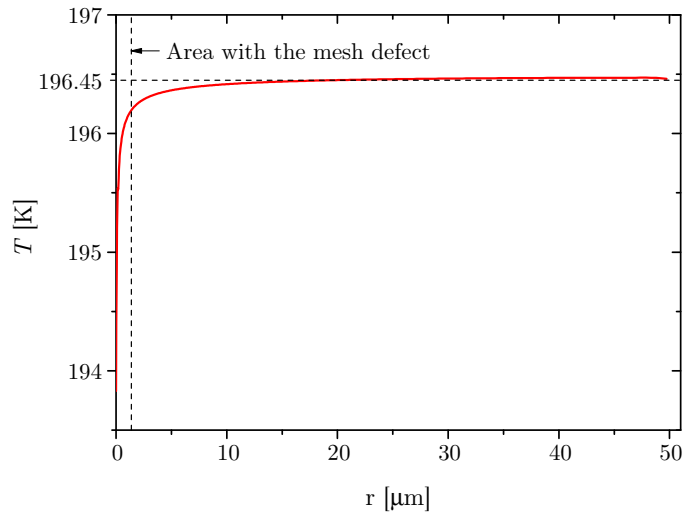


Fig. 4.6: Calculated temperature profile of the spot contact between two glass balls. The border of the small defect for proper meshing is also shown. Apart from the divergence in the area of the defect, the isothermality of the contact was confirmed within 0.3 K.

4.2.3 Model with flat isothermal contact area

Using analytical methods, V. Musilová later validated the isothermality of the contact area for a contact of two identical materials and derived the analytical equation for the model shown in Fig. 4.7.

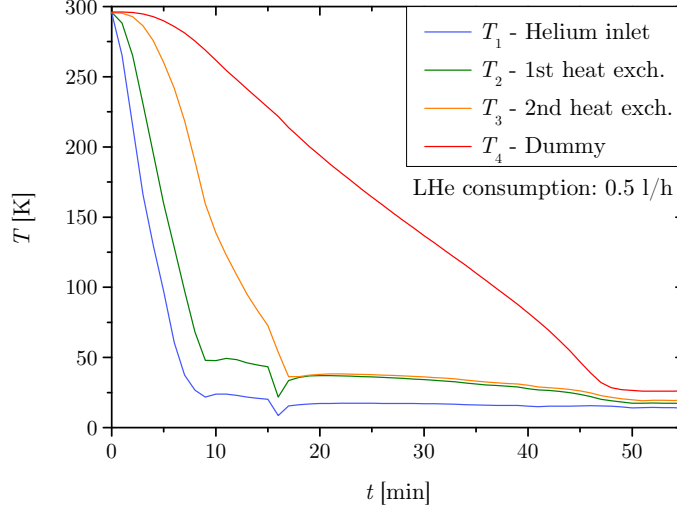


Fig. 4.7: More accurate model for calculation of heat flow through a spot contact. Constant temperature T_1 of the circular spot contact area with radius r_1 is assumed.

Heat flow through the isothermal circular contact to the material with constant thermal conductivity k can be found [22]

$$Q = 4r_1k \cdot (T_2 - T_1). \quad (4.3)$$

V. Musilová showed that this relation can be adapted to the use of temperature dependent thermal conductivity $k(T)$ using so called Kirchhoff transform [23] to the form

$$Q = 4r_1K(T_1, T_2). \quad (4.4)$$

This equation is similar to (4.1), only with the coefficient 4 instead of 2π . The plots in Fig. 4.8 show the comparison of the new model with the numerical simulation and with the measurement. The contact conductivity apparatus and method of measurement is described in my bachelor thesis [4]. The plots show the dependence of the heat flow Q on loading force applied F at the contact for the temperature difference ΔT of 50 K, 100 K, 200 K and 300 K. Naturally, higher the loading force, higher the contact area and thus the heat flow. There is very good agreement of analytical model with the numerical simulations. The experiment confirms the calculation as well. Significant deviation can only be observed for the highest temperature difference of 300 K, where the radiation heat flow in the apparatus becomes significant and was not considered in the calculations.

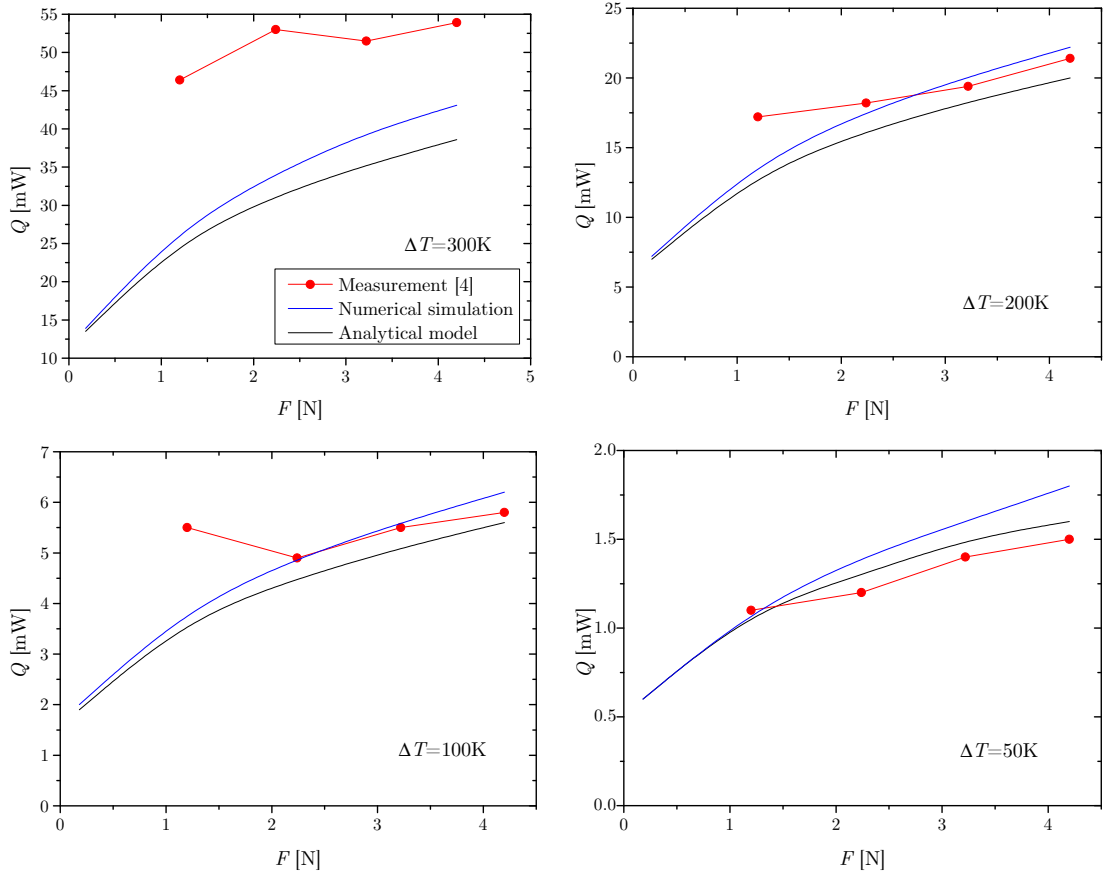


Fig. 4.8: Comparison of the analytical model with flat isothermal area (black line) and the numerical simulation (blue line). Results are also compared with the measurement described in [4] (red circles). Graphs show the dependence of heat flow Q through the spot ball-ball contact on the applied loading force F .

4.3 Testing application of the FBS

Based on the proposed design of the LT-STM described in chapter 2, a model (dummy) of the cooled body representing the sample holder of the STM was created to test the thermal insulation of the bearing with FBS and cooling power of the cryostat. The model, shown in Fig. 4.9, consists of a Al alloy plate (dimensions 30x30x4.5 mm and mass 26 g) placed on FBS. To create a well defined loading force on the supports, the vertical preload of 10 N is applied to the plate via a phosphor bronze plate spring. The fourth FBS is placed underneath the spring to insulate the dummy, because the spring is at room temperature. To monitor and regulate the temperature of the dummy, there is a diode thermometer and a 2 k Ω SMD resistor used as a heater.

The dummy is placed inside the testing vacuum chamber and a strand of high conductive copper wires (i.e. braid) connects the dummy thermally with the heat

exchanger. The braid needs to be thick enough to ensure good thermal connection while still thin enough not to transfer too much vibrations to the sample holder from the heat exchangers. One of the purposes of the following experiments was to test the effectiveness of the heat transfer through it. The thickness of the braid was calculated in such a way so that the dummy would be cooled down under one hour.

In all of the following experiments (except the one in section 4.3.3) the new low-loss transfer line was used and thus much lower LHe throughput was needed in order to keep the heat exchangers at low temperatures.

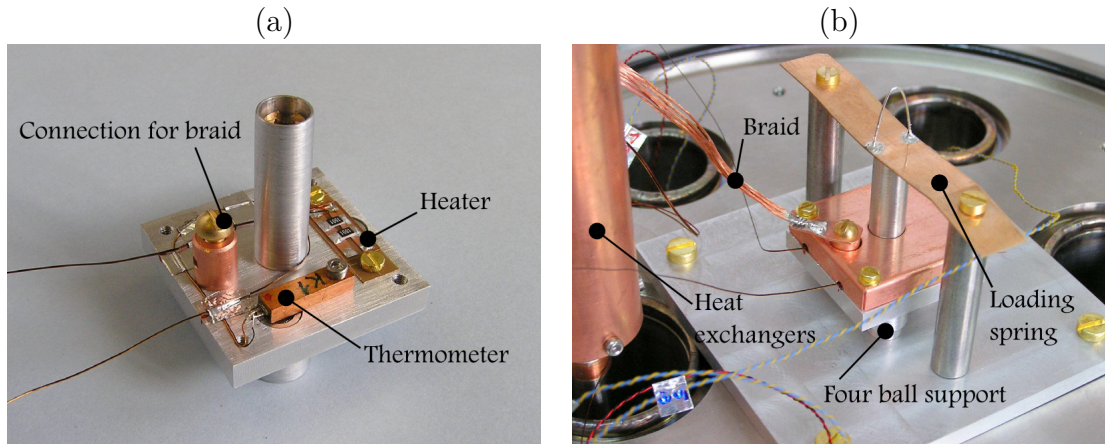


Fig. 4.9: A testing model of the sample holder. (a) View of the model without thermal shielding. The thermometer mount and the heater are shown. (b) Mounted model to the bottom of the vacuum testing chamber and thermally connected to the heat exchanger via copper braid.

4.3.1 Cooldowns

Cooldown time of the setup is definitely an important aspect not only for the convenience of the use (time), but also for the reasonably economical performance (LHe consumption).

Fig. 4.10 shows the typical time behavior of the temperatures on the helium inlet (T_1), both heat exchangers (T_2 and T_3) and the dummy (T_4) during cooldown. With the LHe consumption of 0.5 l/h both heat exchangers cooled down within 20 minutes and the stable temperature of the dummy was reached within 50 minutes. Note that there is only a little additional heat load on the second heat exchanger, since there is no radiation shield around the dummy, and the temperatures of heat exchangers T_2 and T_3 have similar values. Temperature T_3 of the second heat exchanger is about 3 K higher as this heat exchanger is loaded by the radiation to the tube around both heat exchangers. The temperature drop on the braid is about 10 K.

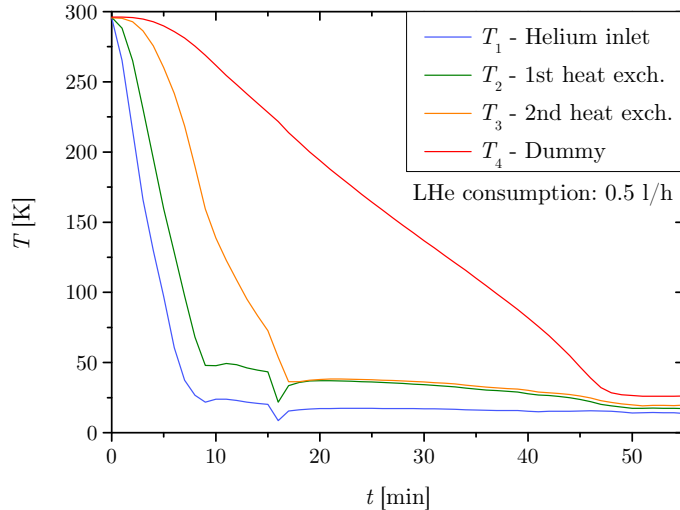


Fig. 4.10: Time dependence of the temperatures during cooldown of the dummy sample holder.

4.3.2 Temperature fluctuations and LHe consumption

The new transfer line with the choking valve inside the Dewar significantly reduced the amplitude of thermal oscillations discussed in the the previous section 3.4.2. However, the oscillations were not suppressed completely and they still occur sometimes with amplitudes on the heat exchangers of even a few Kelvin (the difference between highest and lowest measured value of the period of 30 s is considered as amplitude in this text). Nevertheless, the amplitudes transferred by the braid are much lower. Fig. 4.11 shows the usual waveform of fluctuations for the temperature of the dummy $T_4 = 25$ K. One can see that even when the amplitude of oscillations on the heat exchanger reach 4 K, the dummy's oscillations are less than 60 mK.

The amplitude of oscillations as well as the LHe consumption depend on the convenience of the operation. For each temperature it is possible to reduce the oscillations to minimum and to optimize the helium flow rate by pressurizing the Dewar vessel and fine tuning the valves on the transfer line and on the outlet of the cryostat. Nevertheless, it is obviously less time consuming and more convenient to set a little higher flow rate and regulate the temperature of the dummy by heating. Unfortunately, the used PID controller Lakeshore LS-340 is too slow to dump the oscillations efficiently and is only useful to regulate the mean temperature. When using the controller, long-term temperature stability in range of minutes and more is better than the amplitude of oscillations. Faster controller could possibly damp the oscillations.

Table 4.1 shows the convenient (i.e. not fully optimized) values of LHe consumption and amplitude of oscillations for a few temperatures of the dummy sample holder. Notice how the oscillations lower with increasing the temperature.

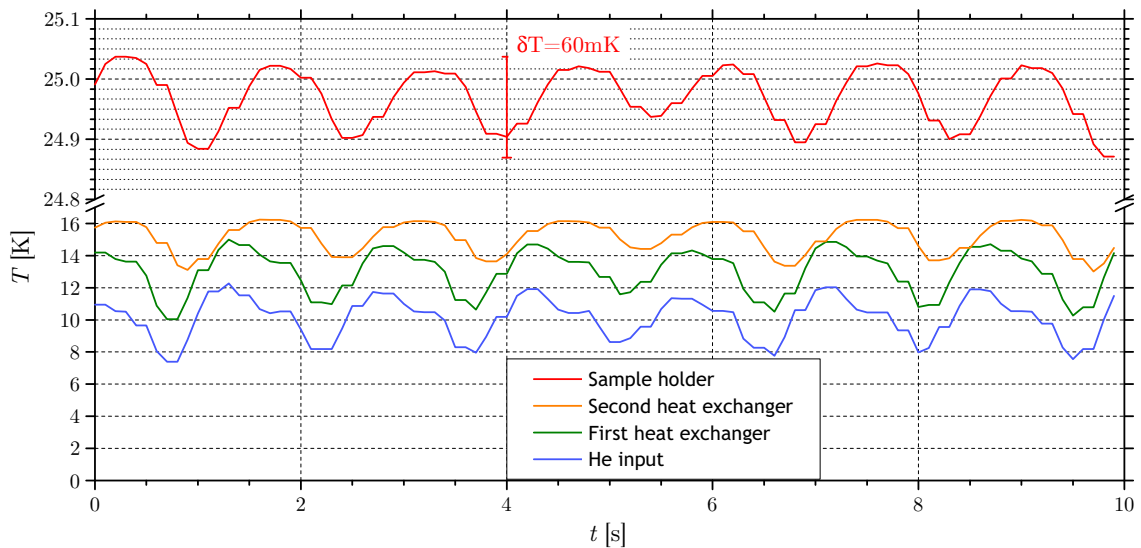


Fig. 4.11: The typical waveform of fluctuations for the temperature of the dummy $T_4 = 25$ K. The oscillations of the heat exchanger reach 4 K while the amplitude on the dummy does not exceed 60 mK.

Tab. 4.1: The convenient not fully optimized values of LHe consumption together with the amplitude of temperature fluctuations for various temperatures of the dummy sample holder.

Dummy temperature T_4 , [K]	Temperature fluctuations δT_4 , [\pm mK]	Consumption LHe, [l/h]
23	202	0.86
25	40	0.80
30	28	0.47
40	33	0.35
50	9	0.32
70	4	0.22

4.3.3 Heat flow analysis

The sample holder dummy also allows to confirm previously calculated heat flow through the FBS in a real scenario of a body fixed by multiple supports. To measure the thermal insulation of the bearing with FBS, a simple substitution method was used. At the first step the temperature of the dummy was set to 44 K and 41 K respectively (the old transfer line was used for this experiment and lower temperatures of the sample holder dummy could not be reached). Once the stable state was set, the temperatures on the heat exchangers and the helium flow rate were measured. Then the whole setup was warmed up and dismantled.

In the second step the preloading spring was taken away and the dummy sample holder was suspended on thin polyester fibers, see Fig. 4.12. Since the thermal conductance of the fibers and of the current leads is negligible, the dummy was not in contact with room temperature parts and only heat radiation affected its temperature. The helium flow rate and the exchanger temperature was adjusted to the same values as in the first step. Obviously, the sample holder dummy reached lower temperature than in the first case, but the temperature was adjusted to the same value as in the first case by heating. The measured heating power substituted the heat flow Q_{FBS} by conduction, so the heat flows are equal.

When the dummy is suspended on the fibers one can determine the radiation heat flow and the conduction of the braid using simple consideration of heat flows in the states with and without heating. Heat flow through the braid equals to the radiation on the dummy and possible heating Q_{q}

$$R + Q_{\text{q}} = \Lambda(T_4 - T_2), \quad (4.5)$$

where Λ is the thermal conductance of braid. There are two unknowns in the equation(4.5): radiative heat flow R and the conduction $\Lambda(T_4 - T_2)$. However, if the temperatures T_2 (first heat exchanger) and T_4 (dummy) in the state with and without heating are similar, thermal conductivity of the braid can be considered constant and we obtain a set of two equations for two unknowns

$$R + 0 = \Lambda \cdot (T_4^{\text{I}} - T_2^{\text{I}}), \quad (4.6a)$$

$$R + Q_{\text{q}} = \Lambda \cdot (T_4^{\text{II}} - T_2^{\text{II}}). \quad (4.6b)$$

Index ^I is for the state without heating and ^{II} for the state with the heating. Solving for Λ we obtain

$$\Lambda = \frac{-Q_{\text{q}}}{(T_4^{\text{I}} - T_4^{\text{II}}) - (T_2^{\text{I}} - T_2^{\text{II}})}. \quad (4.7)$$

Once Λ is known, the radiation heat flow on the dummy sample holder can be estimated

$$R = \Lambda \cdot (T_4 - T_2) - Q_{\text{q}}. \quad (4.8)$$

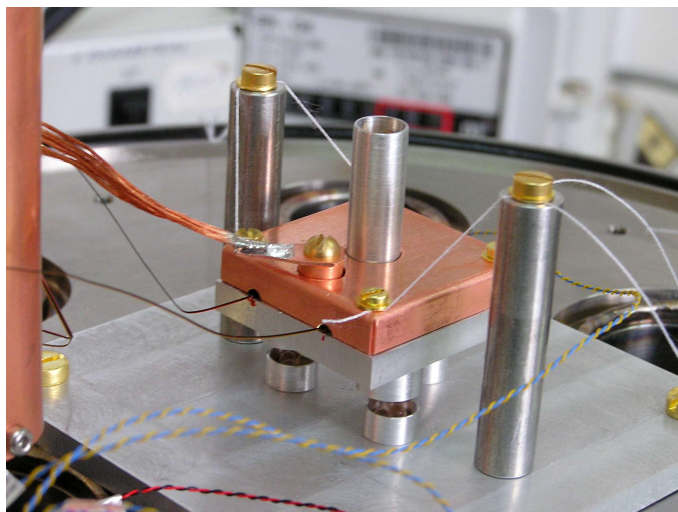


Fig. 4.12: The dummy sample holder suspended on thin polyester fibers used for estimation of the heat conduction through FBS by the substitution method.

The table 4.2 shows the values obtained by the method explained above together with the calculated values. Radiation heat flow was calculated by equation (1.8) for a surface of 37 cm^2 and emissivity of Al alloy to 1%. Conductance Λ of the braid was calculated using previously measured [4] thermal conductivity of the braid's material. In the experiment, the braid consisted of three bundles with 217 strains of $75\text{ }\mu\text{m}$ thick wires and its length was 100 mm.

Tab. 4.2: Measured values of conduction through the complete FBS bearing Q_{FBS} , radiation to the sample holder dummy R and the thermal conductance of the braid Λ . Predicted values from previous calculations are also shown.

	Q_{FBS} [mW]	R [mW]	Λ [mW/K]
calculation	–	84	10.1
measurement	82	113	9.5

4.3.4 Mechanical stiffness measurement

Simple measurement was performed to test the mechanical stiffness of the bearing with FBS. The main purpose of the measurement was to examine the behavior of the bearing under lateral forces, rather than to measure exact mechanical stiffness of the support. The results are very approximative, but some trends could be observed and are described briefly.

Measuring apparatus can be seen on Fig. 4.13. The experiment measures the deflection of the model Δx as a function of lateral force F . The force is applied to the side of the dummy through a wire with spring. The magnitude of the force is regulated with micrometer feed movement and measured with a tension force meter connected to the spring. The deflection of the sample holder dummy is measured with a precise length gauge.

Fig. 4.14 shows the measured dependence of deflection on lateral force for sets of various preloading forces ranging from 5 N to 45 N. Two runs of measurement were performed starting from the lowest force to the highest (first run - filled squares, second run - empty squares). A difference between the runs was observed with a tendency to measure higher stiffness in further runs. We believe that the tendency could be caused by the creation of flat surfaces at the spot contacts by inelastic deformations. The flat spots on the glass spheres could be even observed by the naked eye after the loading the support with the highest preloads. However, such high preloads are not expected to be used in the STM bearing.

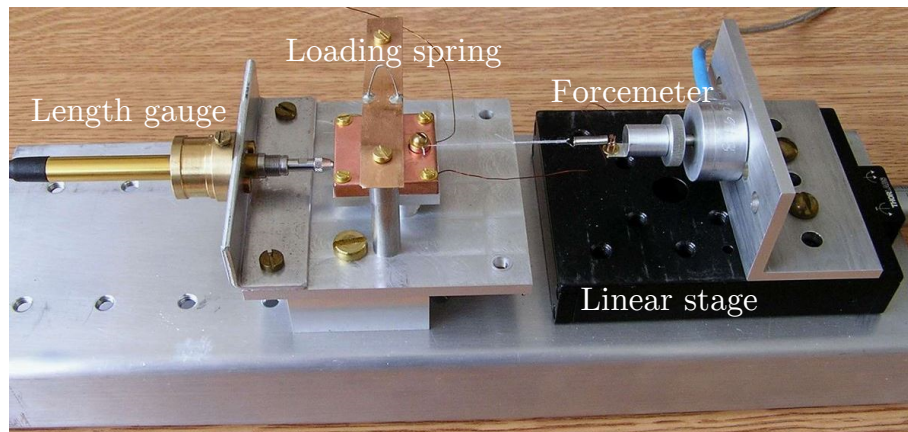


Fig. 4.13: The apparatus for measurement of mechanical stiffness of the bearing with FBS.

As a result, Fig. 4.15 shows the estimated dependence of stiffness K on the preload F_P from calculation of the linear regression. The scatter in data is rather large, but it gives some rough estimation of mechanical stiffness of the bearing using FBS.

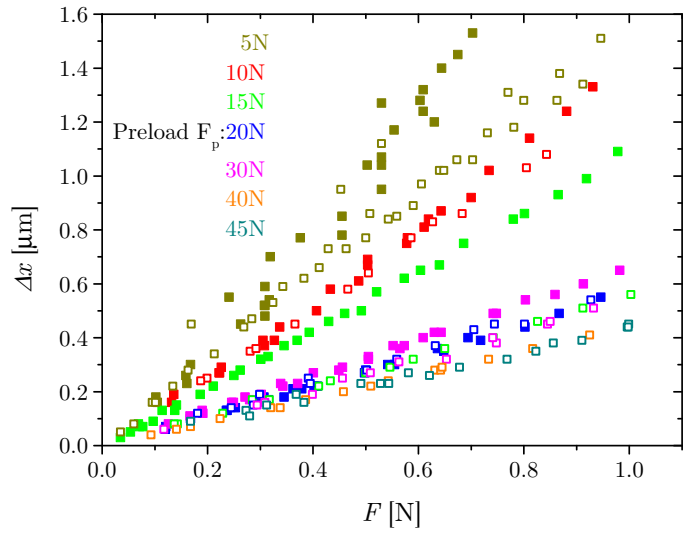


Fig. 4.14: Measured dependence of deflection Δx of the sample holder dummy on lateral force F for various preloading forces F_p (from 5 N to 45 N). Two runs of measurements are shown: first run with full squares and second with empty squares.

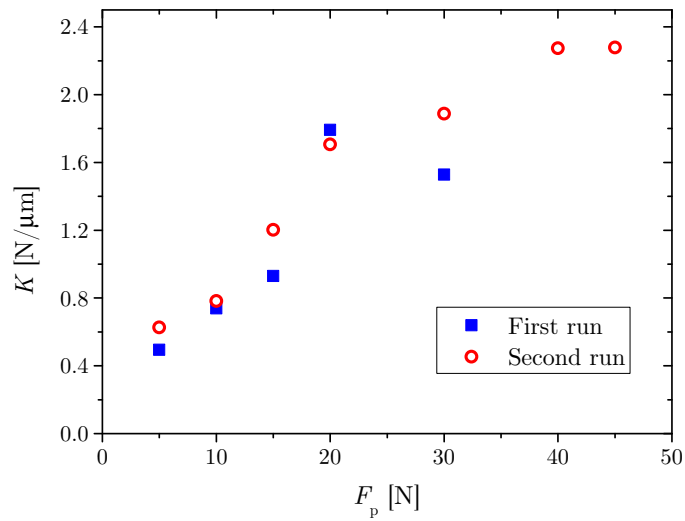


Fig. 4.15: Measured dependence of mechanical stiffness K on the preload F_p .

5 NEW DESIGN OF THE STM PLATFORM

The previous concept of the STM platform mentioned in chapter 2 included a cooled sample holder and a scanning head at room temperature. The new solution involves cooling both the sample holder and the scanning head tightly embedded inside a copper block. The reason of this change is that no mutual thermal insulation of the two pieces is needed and a very rigid connection is secured. This leads to significant reduction of tip-to-sample vibrations. The new design also requires new STM scanning head that can operate at low temperature.

Fig. 5.1 shows the proposed setup. The hollow copper block with the scanning head and the sample holder (named as the “core” in the following text) is placed on three FBSs discussed in chapter 4 that insulate it from the table at room temperature. Since the FBSs need to be preloaded, there are three thin stainless steel wires pulling the microscope to the table. These wires however also transfer heat from the table and they need to be sufficiently long to reduce their conductance. Therefore, each wire is anchored to a thin-walled stainless steel tube. In addition, the tubes also hold the radiation shield around the core.

Unfortunately, the new concept imposes new difficulties for the cryogenic part. The mass of the cooled object in the new design reaches 450 g compared to 26 g of the studied sample holder dummy arising from the first concept. The copper body of the microscope is about 50 mm in diameter and 70 mm in height. The main difficulty is a big surface area which needs to be shielded against radiation and, even more importantly, high heat capacity of the cooled object. In this chapter a solution of mounting the core at cryogenic temperature on the table at room temperature is proposed and the supporting calculations of the heat flows and cooldown time are described. The design of the platform is preliminary, and will be developed further. At this moment, careful vibration analysis of the proposed setup is needed and will be performed at the IPE. Conclusions of the analysis might lead to another change in the design. Nevertheless, the method of calculations was established and the results will serve as a base for further solutions.

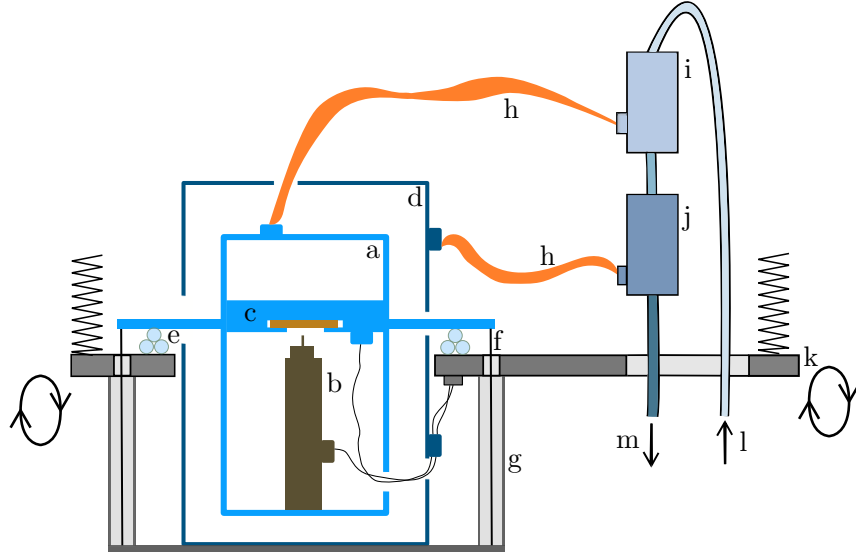


Fig. 5.1: Schematic representation of the new LT-STM platform. Scheme shows: (a) cooled STM core, (b) scanning head, (c) sample holder, (d) radiation shield, (e) four ball supports, (f) stainless steel wire, (g) thin-walled stainless steel tube (h) copper braids, (i) colder core heat exchanger, (j) warmer shield heat exchanger, (k) table with springs and electromagnetic damping, (l) cold He inlet, (m) warm He outlet.

5.1 Steady state heat flow calculation

The procedure of the calculation is as follows. First, it is necessary to estimate the temperatures of the heat exchangers T_{V1} and T_{V2} , radiation shield T_S and the core T_C . The previous experience gained in experiments with the sample holder dummy (chapter 4) was used here. Then all of the individual heat flows shown in Fig. 5.2 are calculated. In thermal equilibrium, all parasitic heat flows are drained to the heat exchangers either by the braid connected to the core or by the braid connected to the radiation shield and thus we can write

$$Q_C = Q_{HC} + Q_{WC} + Q_{KC} + Q_{CC} + Q_{RC}, \quad (5.1a)$$

$$Q_S = Q_{RS} + Q_{CS} + Q_{WS} + Q_{HS} - Q_{RC} - Q_{WC} - Q_{CC}, \quad (5.1b)$$

where Q_C and Q_S are total heat flows to the core and radiation shield respectively. The description of each of the partial heat flows can be found in tables 5.3 and 5.4 for quick orientation.

Radiation heat flows

Both the shield and the metallic block inside it (the core) will be made of chemically polished copper and the constant, temperature independent emissivity of $\varepsilon = 0.5\%$

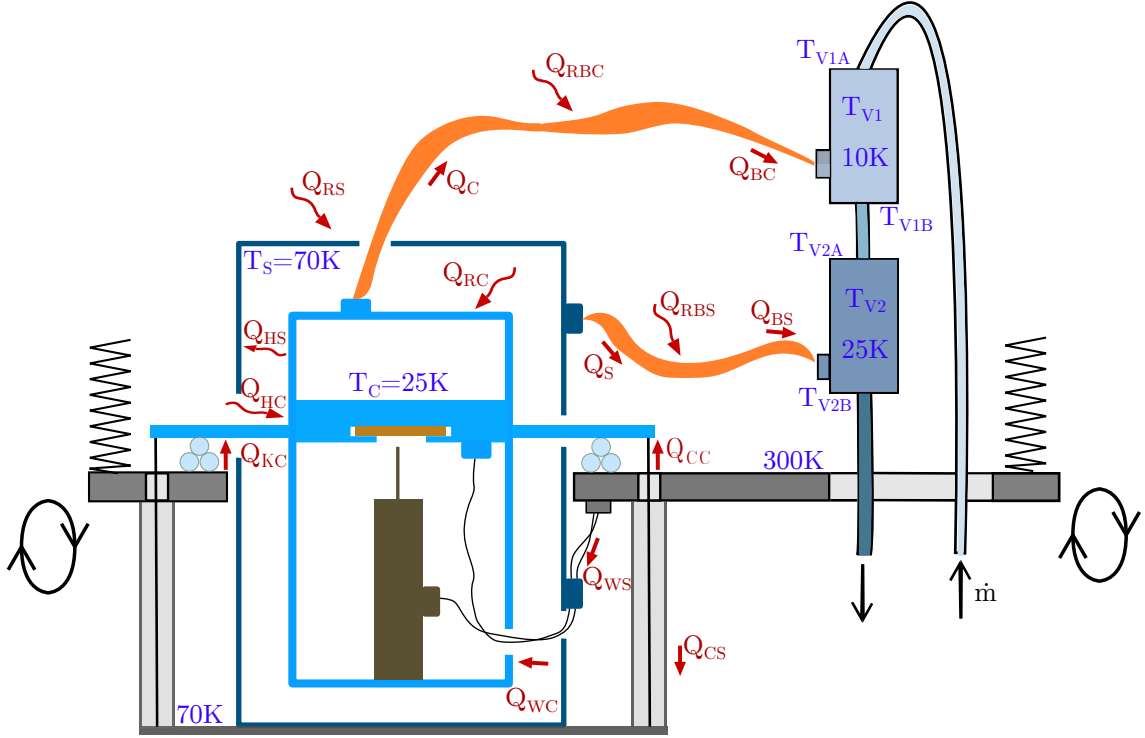


Fig. 5.2: The scheme of the new calculated model. All calculated heat flows are shown together with the temperatures for which are the flows evaluated in this text.

of both surfaces is used for further calculations. The calculations assume total surface area of the shield to be equal to that of the core and the value of $S = 220\text{ cm}^2$ is used. Naturally, in reality the surface of the radiation shield will be slightly bigger, but for the purpose of these calculations the areas can be considered the same with acceptable error.

- *Radiation to the core from T_S :* Q_{RM}

For the calculation of the radiation heat flow between the surfaces of the same surface area, the equation (1.5) and the condition (1.7b) is used.

- *Radiation to the shield from 300 K:* Q_{RS}

Due to the fact that the vacuum chamber surrounds the shield and its surface is much greater than that of the radiation shield, the equation (1.10b) is used in this case.

- *Radiation from 300 K through the openings in the shield:* Q_{HC} and Q_{HS}

Naturally, the radiation shield can never completely surrounds the core. For constructional reasons, a few openings are necessary in the shield (for electrical leads, supports etc.). For the calculation of the radiation heat flow through the openings Q_H , we assume that all the room temperature radiation is absorbed on the surfaces inside the shield and use the equation (1.11). Because the emissivities and the surface of the shield and of the core are considered to be equal, both surfaces will

absorb one half of the total radiation heat flow Q_H

$$Q_{HC} = Q_{HS} = Q_H/2. \quad (5.2)$$

We assume that holes in the radiation shield cover 2.5% of shielding, which corresponds to about $S = 5.7 \text{ cm}^2$ of the surface area. This heat flow is the highest of all in case of the core (see Tab. 5.3). To lower the Q_{HC} , the inside walls of the radiation shield should be covered by a material with absorbtivity coefficient close to unity. Then we could assume that a significant part of the radiation is reflected by the copper core and absorbed by the shield. However, it is not trivial to find a material with high value of absorbtivity and UHV compatibility.

Conduction heat flows

All conduction heat flows were calculated using equation (1.13). Temperature dependent thermal conductivity for the materials of the wires was found using commercial software Cryocomp [12]. The program enables to calculate various physical characteristics of more than 60 materials in a temperature range from 1 K to 300 K. For calculation of the conduction heat flows through the parts with temperature dependent thermal conductivity with the possible radiation from the surroundings, program KRYOM 3.3 [18] was used.

- *Conduction through the stainless steel tubes: Q_{CS}*

The length of the stainless steel tube is 70 mm, outer diameter 3 mm and wall thickness 0.25 mm. One end is attached to the table at 300 K and the other holds the shield (at temperature T_S). Room temperature radiation heat flow from the vacuum chamber on the tube with absorptivity of 6% (stainless steel) is also included.

- *Conduction through the stainless steel wires: Q_{CC}*

There are three wires creating preload on the FBS with one end at the temperature T_C and other connected to the stainless steel tube at temperature T_S . The length of the stainless steel wire is 90 mm and the diameter only 0.2 mm. Such a thin wire is sufficient, because of high yield stress value of stainless steel. The highest loads on each of the wire are expected not to exceed 10 N. The wire is exposed to the radiation from the vacuum chamber or from the stainless steel tube with varying temperature from T_S to 300 K. To simplify the calculation, we assume the wire is exposed to 300 K radiation on the whole length with emissivity of the stainless steel of $\varepsilon = 6\%$.

- *Conduction through the FBSs: Q_{KC}*

Conduction through the supports was measured with the sample holder dummy discussed in section 4.3.3. Three FBSs are utilized in this design.

- *Conduction through electric leads: Q_{ws} and Q_{wc}*

The choice of the electrical wires play significant role in the LT-STM, because many leads are needed (piezoelectric scanners, thermometers, tunneling current wires etc.) and the parasitic heat flow through them is not negligible. The values of the total conduction heat flow through the wires in tables 5.3 and 5.4 are very approximate and depend on the final choice of the wires, their length and their quantity. Therefore, tables 5.1 and 5.2 give an overview of calculated parasitic heat flows through some commercially available low-conduction cryogenic wires and shielded coaxial cables for the length of 100 mm. Naturally, the wires leading to cooled core will be thermally anchored to the radiation shield, thus two heat flows Q_{ws} (from 300 K to 70 K) and Q_{wc} (from 70 K to 25 K) are calculated.

It is evident that copper wires should be avoided due to their very high thermal conductivity if not absolutely necessary. Copper alloys such as mentioned phosphor bronze offer a good compromise between low thermal conductivity and low electrical resistance. The signal leads often need electrical shielding and a mini-coaxial cables are a good choice.

Tab. 5.1: Parasitic heat flow calculation for some commercially available cryogenic wires for the length of 100 mm. Conduction through the insulation material was neglected.

Type	Comments	Material	Q_{ws} [mW]	Q_{wc} [mW]
KAPW1X015 ¹	ø150 μm, single wire	Cu	15	9.6
DT-36 ²	ø127 μm, 2 twisted	Phosphor bronze	2.6	0.3
MW-36 ²	ø127 μm, single wire	Manganin	0.5	0.1

Tab. 5.2: Parasitic heat flow calculation for some commercially available cryogenic mini-coaxial cables for the length of 100 mm. Conduction through the wire and the shielding is included.

Type	Conductor	Shielding	Q_{ws} [mW]	Q_{wc} [mW]
SC ²	ø180 μm stranded Cu	braided copper	125	80
SS ²	ø180 μm stainless steel	braided stainless	3.0	0.5
02-32-013 ³	ø200 μm stainless steel	braided stainless	10	1.6

Optimization of the braids

Once the total heat flows Q_C and Q_S are known, the cross-sectional area of the braids is calculated to conduct these heat flows to the heat exchangers. The room temperature radiation to the braids needs to be assumed as the braids are not shielded. Thus we obtain

$$Q_{BC} = Q_C + Q_{RBC}, \quad (5.3a)$$

$$Q_{BS} = Q_S + Q_{RBS}, \quad (5.3b)$$

where Q_{BC} and Q_{BS} are the final heat loads at the heat exchangers.

Both absorptivity and the surface area of the braid are difficult to estimate correctly. We suppose that the absorptivity of individual wires is 5%. Moreover, the uncertainty in the surface area exposed to the room temperature radiation is even higher. The braid consists of bundles containing 217 individual fine wires in

¹LewVac Components, Ltd.

²Lake Shore Cryotronics, Inc.

³CMR-Direct, Hertford Developments, Ltd.

each bundle, with diameter of the single wire of $75\ \mu\text{m}$ [4]. To minimize the vibration transfer from the heat exchangers, the braid should be unraveled to the individual wires. However, when the braid is unraveled it collects much more radiation due to the increase in the outer surface area. Three bundles of fine wires were used in the experiments with sample holder dummy. There are two extreme cases: If we assume the braid as a simple rod, we obtain the circumference of the braid of $5.9\ \text{mm}$. If we sum up the circumferences of all wires, we obtain the value $150\ \text{mm}$ changing the previous value by the factor of 25. Naturally, the solution is to use the unravelled braid while keeping the wires close together, but the actual surface area can only be guessed. For the heat flows mentioned in this section we assumed that 20% of the total surface of the individual wires is exposed to the room temperature.

Experimentally found thermal conductivity of the braids was used (the Residual Resistance Ratio of the braid is 64), details can be found in [4]. From calculations in Kryom 3.3 [18] we obtain that for the length of $100\ \text{mm}$ both braids need to consist of at least 2 bundles of fine wires with total cross-sectional area of $1.92\ \text{mm}^2$ for each braid.

LHe consumption estimation

Finally, using equation (3.1), minimal helium mass flow rate and the corresponding LHe consumption through each of the heat exchangers is calculated with given inlet and outlet temperatures on both heat exchangers T_{V1A} and T_{V1B} (or T_{V2A} and T_{V2B} respectively, see Fig. 5.2). We suppose that the temperatures of the heat exchangers are equal to the helium gas leaving them and that the helium does not warm up between the heat exchangers

$$T_{V1} = T_{V1B} \quad , \quad T_{V2} = T_{V2B}, \quad (5.4a)$$

$$T_{V1B} = T_{V2A}. \quad (5.4b)$$

We alter the temperatures of the shield and the core until the flow rate through both heat exchangers is similar. As mentioned in section 3.4.2, the parasitic heat loss in the transfer line is almost $900\ \text{mW}$. Based on the experience with previous tests of the heat exchangers (sections 3.4.3 and 4.3.1), throughput of at least $0.51/\text{h}$ of LHe is needed to keep the temperature of the helium entering the first heat exchanger under $5\ \text{K}$. Ideally, we want to calculate a mass flow rate that does not exceed this value.

The tables 5.3 and 5.4 below summarize all calculated heat flows to the radiation shield and to the core for one set of temperatures. In all of the calculations mentioned in this section the temperature of the core T_C is assumed to be $25\ \text{K}$ and the shield temperature T_S is $70\ \text{K}$, as it apparent from Fig. 5.2.

Tab. 5.3: Calculated parasitic heat flows on the STM core. The LHe consumption estimated from the total heat load is also shown.

Notation	Description	Q
Q_{HC}	Absorbed radiation through the holes in the shield	131 mW
Q_{WC}	Electrical wires conduction	67 mW
Q_{KC}	3x FBS conduction	57 mW
Q_{CC}	Stainless steel wires conduction	5 mW
Q_{RC}	Radiation from the shield	0.1 mW
Q_C	Total heat load on core	260 mW
Q_{RBC}	Radiation to the braid	19 mW
Q_{BC}	1st heat exchanger heat load	279 mW
	LHe consumption for $T_{V1B} - T_{V1A} = 5$ K	0.331/hod

Tab. 5.4: Calculated parasitic heat flows to the radiation shield. The LHe consumption estimated from the total heat load is also shown.

Notation	Description	Q
Q_{CS}	Stainless steel tubes conduction	299 mW
Q_{CC}	Stainless steel wires conduction to the core	-5 mW
Q_{WS}	Electrical wires conduction from 300 K	172 mW
Q_{WC}	Electrical wires conduction to the core	-67 mW
Q_{HS}	Reflected radiation through holes in the shield	131 mW
Q_{RS}	Radiation to the shield from 300 K	50 mW
Q_{RC}	Radiation to the core	-0.1 mW
Q_S	Total heat load on the shield	580 mW
Q_{RBS}	Radiation to the braid	19 mW
Q_{BS}	2nd heat exchanger heat load	599 mW
	LHe consumption for $T_{V2B} - T_{V2A} = 15$ K	0.251/hod

5.2 Cooldown time calculation

After a suitable solution for the steady state is found, it is important to check the cooldown time of such setup. A limit of two hours was settled as a maximum time for the apparatus to reach its lowest temperature. From section 4.3.1 we know it took around 20 minutes to cool the heat exchangers and about 50 minutes to cool down the sample holder dummy. However, the dummy's mass was about 26 g (mostly made of aluminum alloy) whereas the STM core's mass will be about 450 g mostly composed of copper and titanium. The temperature dependence of the heat capacity of the core consisting of its copper and titanium parts in comparison with the capacity of the sample holder dummy is shown in Fig. 5.3. The capacity of the STM core is more than 6 times higher than that of the dummy at room temperature and more than 8 times higher for temperatures below 50 K.

The program USTAL [24] developed at the ISI was used. The program numerically calculates a time dependence of the temperature of a cooled body and heat flows through the thermal links to its surroundings. The calculation includes the temperature dependence of the thermal conductivity of the thermal bond, the temperature dependent heat capacity of the sample and heat radiation from surroundings. However, heat capacity of the thermal link is not included. In our case, we calculate the cooldown time t_C and the final reached temperatures T_C for the STM core with known heat capacity, geometry and thermal conductivity of the braid, conductance of the supports and for the constant temperature of the heat exchanger T_{V1} . Only the calculated temperature T_C can be time dependent, so the temperature of the heat exchanger and radiation shield must be assumed constant.

The lowest temperature and the cooldown time strongly depend on the radiation heat flow to the braid, which was discussed in previous section 5.1. The table 5.5 summarizes the cooldown times t_C as well as the reached temperature T_C for a few configurations varying thickness of the braid characterized by the number bundles N , its length l , absorptivity a and the fraction of surface exposed to the room temperature radiation S_{Rad} .

In the steady state calculation was found that for a length of 100 mm 2 bundles of fine wires are sufficient to drain all parasitic heat flows and keep the STM core at 25 K for the temperature of heat exchanger at 10 K and shield at 70 K. However, the results in table 5.5 show that using a thin braid would result in an unacceptable cooldown time of more than 7 h. To reduce the cooldown time under 2 h, at least three times as thick braid is needed. Braid consisting of 8 bundles would be better, due to the uncertainty in radiation heat flow mentioned earlier. If the longer braid with length of 150 mm is permissible, then at least 10 bundles will be required to cool down the STM core under 2 h. Nevertheless, a study of vibration transfer the

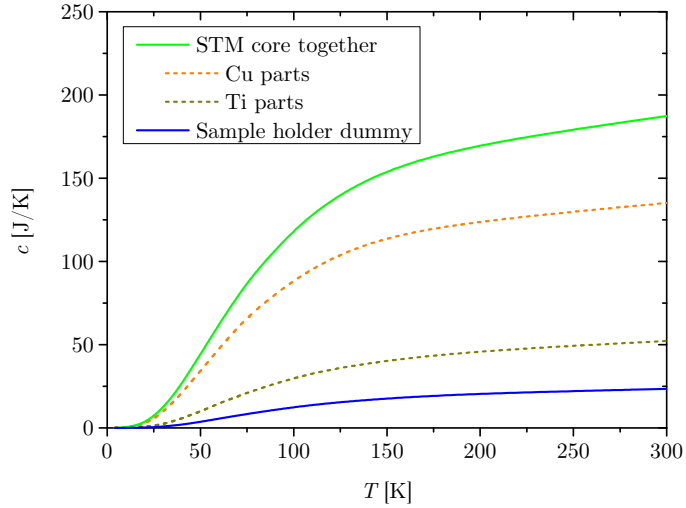


Fig. 5.3: Comparison of the heat capacity of the sample holder dummy and the STM core. Partial heat capacities of the STM core parts made of Ti and Cu are also shown. Temperature dependence of heat capacity was found using the Cryocomp software [12].

braid is missing. The results of such study will surely settle limitations of maximum braid thickness and its minimum length.

Cooldown time calculation of the radiation shield was not performed, because the shield will have much lower heat capacity and it also operates at higher temperature. Moreover, we suppose that the transfer of vibrations to the shield is not as critical as to the STM core, so the braid can be thicker if necessary.

Tab. 5.5: Calculated cooldown times t_C and final temperatures T_C of the STM core for various configurations of the braid. N is the number of bundles the braid consists of, l is the length of the braid and S_{Rad} is the fraction of braid's surface exposed to the room temperature radiation.

N []	l [mm]	S_{Rad} [%]	T_C [K]	t_C [h]
2	100	20	28.5	7.3
4	100	20	20.9	3.1
5	100	20	19.3	2.4
6	100	20	18.2	2.0
7	100	20	17.3	1.7
8	100	20	16.6	1.5
8	150	20	20.0	2.3
8	200	20	23.5	3.3
8	100	50	18.1	1.5
8	100	100	20.4	1.6
9	100	20	16.2	1.3
9	150	20	19.3	2.1
10	150	20	18.7	1.8

6 CONCLUSIONS

Considering the requirements of the Scanning probe microscopy group at the Institute of Physical Engineering (IPE) at Brno University of Technology, two versions of the low temperature STM platform with flow cooling system using cryogenic helium were designed. First, a version of the STM platform with the cooled sample holder and scanning head at room temperature was studied. Based on this setup, a flow cooling system was designed consisting of a helium flow cryostat, a Dewar vessel with liquid helium (LHe) and a low-loss transfer line. The cryostat is composed of He inlet/outlet, heat exchangers and copper braids for the thermal connection of both the sample holder and the radiation shield around it with the heat exchangers. The calculations preceding the realization are explained and the implications of the results on the design are commented. The cooling system was experimentally tested and used to cool down the model of the sample holder in a testing vacuum chamber designed and built for this purpose. During the tests, the temperature of the sample holder model of 20 K was reached with the LHe consumption of 1.5l/h and 25 K with 0.6l/h.

The study of the thermally insulating four ball supports with contacts of glass spheres [4] was continued focusing on estimation of the heat flow through a spot contact both analytically and numerically. The application of the supports for mounting the cooled parts of the STM on the table at room temperature was tested with the model of the sample holder. Using the supports, the measured conductive heat flow from 300 K to 40 K is less than 100 mW without compromising on mechanical stiffness of the mount. The four ball supports are universal and can be used for any application where low thermal conductance, mechanical stiffness and small dimensions are desired. The idea, analysis and experimental results were summarized in an article and submitted to a scientific journal for publication [5].

Finally, the second version of the STM platform, characterized by cooling both the STM scanning head and the sample holder enclosed in a copper block is introduced. A solution of mounting of the block and the surrounding radiation shield on the table is proposed and a complex analysis of the heat flows in this system is performed. Moreover, the cooldown time of the copper block with STM was estimated for various thicknesses and lengths of the braid. At this moment, careful vibration analysis of the proposed setup is needed and will be performed at the IPE. Conclusions of the analysis might lead to another changes in the design. Nevertheless, the method of calculations was established and the results will serve as a base for further solutions.

BIBLIOGRAPHY

- [1] Janis Research, Co., *ST-400UHV Cryostat*. <http://www.janis.com/>.
- [2] Omicron Vakuumphysik GMBH, *The 25 – 1500 K Variable Temperature UHV SPM*. <http://www.omicron.de>.
- [3] RHK Technology, Inc., *Variable Temp BEETLE™*. <http://rhk-tech.com/>.
- [4] J. Voňka, “Materials and their application in low temperature parts of STM microscope,” Master’s thesis, Brno University of Technology, Faculty of Mechanical Engineering, 2011.
- [5] P. Hanzelka, J. Vonka, and V. Musilova, “Low conductive support for thermal insulation of a sample holder of a variable temperature scanning tunneling microscope,” *Rev. Sci. Instrum.*, In review.
- [6] J. Jelínek and Z. Málek, *Kryogenní technika*. SNTL Praha, first ed., 1982.
- [7] F. Pobell, *Matter and Methods at Low Temperatures*. Springer London, third ed., 2007.
- [8] E. W. Lemmon, M. L. Huber, and M. O. McLinden, *NIST Standard Reference Database 23: Reference Fluid Thermodynamic and Transport Properties - REFPROP*. National Institute of Standards and Technology, Standard Reference Data Program, Gaithersburg, 9.0 ed., 2010.
- [9] R. Barron, *Cryogenic Heat Transfer*. Taylor & Francis, 1999.
- [10] V. Musilova, T. Kralik, P. Hanzelka, and A. Srnka, “Effect of different treatments of copper surface on its total hemispherical absorptivity bellow 77K,” *Cryogenics*, vol. 47, no. 4, pp. 257 – 261, 2007.
- [11] V. Musilova, P. Hanzelka, T. Kralik, and A. Srnka, “Low temperature radiative properties of materials used in cryogenics,” *Cryogenics*, vol. 45, no. 8, pp. 529 – 536, 2005.
- [12] The CryoComp Package, Version 3.0. Florence, SC, USA: Eckels Engineering Inc., 1997.
- [13] P. Hanzelka, V. Musilova, T. Kralik, and J. Vonka, “Thermal conductivity of a CuCrZr alloy from 5K to room temperatures,” *Cryogenics*, vol. 50, no. 11 - 12, pp. 737 – 742, 2010.
- [14] C. Kittel, *Introduction to Solid State Physics*. John Wiley & Sons, 2004.

- [15] R. Scott, *Cryogenic engineering*. Van Nostrand, 1959.
- [16] R. Vance, *Cryogenic technology*. University of California engineering and physical sciences extension series, John Wiley & Sons, 1963.
- [17] J. Nekula, “Návrh rastrovacího tunelovacího mikroskopu STM,” Master’s thesis, Brno University of Technology, Faculty of Mechanical Engineering, 2004.
- [18] P. Hanzelka and I. Vejchoda, “Kryom (Version 3.3). [Software]. Institute of Scientific Instruments, Brno, CR.,” 1998.
- [19] J. Weisend, *Handbook of Cryogenic Engineering*. Taylor & Francis, 1998.
- [20] S. Černochoch, *Strojně technická příručka*. No. 1, SNTL - Nakladatelství technické literatury, 1968.
- [21] V. Musilova, J. Dupak, P. Hanzelka, T. Kralik, and P. Urban, “Economical helium bath cryopump: design and testing,” *Vacuum*, vol. 74, no. 1, pp. 77 – 83, 2004.
- [22] H. Carslaw and J. Jaeger, *Conduction of heat in solids*. Oxford science publications, Clarendon Press, 2nd ed., 1959.
- [23] L. Jiji, *Heat Conduction*. Springer-Verlag, 2009.
- [24] P. Hanzelka, “Ustal (Version 4). [Software]. Institute of Scientific Instruments, Brno, CR.,”

LIST OF SYMBOLS, PHYSICAL CONSTANTS AND ABBREVIATIONS

a	Absorptivity	[-]
c	speed of light	[m s ⁻¹]
c_p	specific heat at constant pressure	[J kg ⁻¹ K ⁻¹]
c_v	molar specific heat at constant volume	[J mol ⁻¹ K ⁻¹]
d	diameter	[m]
E_{21}	Mutual emissivity	[-]
E_λ	monochromatic emissive power	[W m ² μm ⁻¹]
F	force	[N]
h	Planck constant	[J s]
\hbar	Planck constant	[J s]
k	thermal conductivity	[W K ⁻¹ m ⁻¹]
k_B	Boltzmann constant	[m ² kg s ⁻² K ⁻¹]
l	length	[m]
m	mass	[kg]
\dot{m}	mass flow rate	[kg s ⁻¹]
N_A	Avogadro constant	[mol]
Nu	Nusselt number	[-]
p	pressure	[Pa]
Pr	Prandtl number	[-]
r	radius	[m]
R	ideal gas constant	[J mol ⁻¹ K ⁻¹]
Re	Reynolds number	[-]
S	cross-sectional area	[m ²]

t	time [s]
T	temperature [K]
T_F	Fermi temperature [K]
u_d	velocity of gas [m s^{-1}]
Q	heat flow [W]
α	coefficient of thermal expansion [K^{-1}]
α_h	heat transfer coefficient [-]
ε	Emissivity [-]
η	Dynamic viscosity [$\text{kg m}^{-1} \text{s}^{-1}$]
Θ_D	Debye temperature [K]
λ	wavelength [m]
Λ	conductance [W K^{-1}]
ν	Poisson's ratio [-]
ν_{kin}	kinematic viscosity [$\text{m}^2 \text{s}^{-1}$]
ξ	pressure loss coefficient [-]
ρ	density [kg m^{-3}]
σ	Stefan-Boltzmann constant [$\text{W m}^{-2} \text{K}^{-4}$]
ω	frequency [s^{-1}]